

High-energy gamma-rays and neutrons observed in very impulsive solar flare on 2012 June 3

Kohki KAMIYA,^{1,*} Kiyokazu KOGA,¹ Satoshi MASUDA,²
Haruhisa MATSUMOTO,¹ Yasushi MURAKI^{ID},^{2,*} Osamu OKUDAIRA,³
Shoichi SHIBATA,⁴ Hiroyasu TAJIMA,² Yasuyuki TANAKA,⁵
Tokonatu YAMAMOTO,⁶ and Kyoko WATANABE⁷

¹JAXA, Tsukuba Space Center, 2-1-1 Sengen, Tsukuba, Ibaragi 305-8505, Japan

²Institute for Space-Environment Research, Nagoya University, Furo-cho, Chikusa-ku, Nagoya, Aichi 464-8601, Japan

³Planetary Exploration Research Center, Chiba Institute of Technology, 2-17-1 Tsudanuma, Narashino, Chiba 275-0016, Japan

⁴Engineering Science Laboratory, Chubu University, 1200 Matsumoto-cho, Kasugai, Aichi 487-8501, Japan

⁵Department of Physics, Hiroshima University, 1-3-1 Kagamiyama, Higashihiroshima, Hiroshima 739-8526, Japan

⁶Department of Physics, Konan University, 8-9-1 Okamoto, Higashinada, Kobe, Hyogo 658-0027, Japan

⁷National Defense Academy, 1-10-20 Hashirimizu, Yokosuka, Kanagawa 239-8686, Japan

*E-mail: kamiyar1@yahoo.co.jp, muraki@isee.nagoya-u.ac.jp

†Former address: JAXA.jp; present address: Institute for Q-shu Pioneer of Science, Rengo-Fukuoka-Tenjin building 5F, 1-15-35 Tenjin, Fukuoka 810-0001, Japan

Received 2021 May 6; Accepted 2021 September 1

Abstract

An impulsive solar flare was observed on 2012 June 3 by the Geostationary Operational Environment Satellite. In this flare, a salient feature was recognized whereby high-energy ions were accelerated to a few GeV within one minute. Associated with this flare, high-energy gamma-rays as well as high-energy neutrons were detected by the Space Environment Data Acquisition equipment onboard the International Space Station. A remarkable feature found of this event was an exceedingly high n/γ -ratio observed between the intensities of high-energy neutrons and gamma-rays. To understand a high n/γ -ratio of about 600, the interaction processes between the accelerated ions and ambient solar atmosphere were simulated for various test cases, taking into account the magnetic field of the photosphere. The simulation was extended by using the GEANT4 code and it was shown that the observed results could be reproduced under certain conditions selected for the actual interaction process. The results suggest that helium and C, N, and O ions were predominantly accelerated in this flare, and that high-energy gamma-rays and neutrons were produced by interactions between the accelerated ions and the ambient gas. As a result, a high n/γ -ratio was produced.

Key words: acceleration of particles — Sun: flares — Sun: particle emissions

1 Introduction

1.1 Understanding the origin of solar cosmic rays

It has been known since 1942 that high-energy particles are emitted in solar flares (Forbush 1946). They are known as Solar Energetic Particles (SEP) (Cane 2000; Ryan et al. 2000) or Solar Cosmic Rays (SCR) (Miroshnichenko 2015). Some protons with energies over 30 GeV have been observed (Miroshnichenko 2015), but how solar plasma is accelerated to such high energies remains unknown. A search for a solution to this question has been ongoing since 1990 (Chupp 1971; Dorman 2010) based on the neutron channel. This paper begins its study of the origin of SCRs by introducing the advantages and disadvantages of neutron observations compared to gamma-ray observations.

Accelerated electrons with an energy of 100 MeV sometimes emit gamma-rays by the bremsstrahlung process. On the other hand, accelerated ions produce gamma-rays at around 100 MeV. Neutral pions are produced by the nuclear interactions of these high-energy ions with the nuclei of the solar atmosphere, but they immediately decay into two gamma-rays. The energy spectrum of these gamma-rays usually has a peak at 70 MeV corresponding to half the mass of a neutral pion (~ 135 MeV). It is hard to distinguish from data analysis whether a gamma-ray originated from an electron or ion process. Neutrons, however, are produced only by nuclear interactions of ions, so it can be said with certainty that they result from ions accelerated to high energies in the impulsive flare.

Of course, knowledge of high-energy charged particles such as protons, helium nuclei, and iron nuclei is important for understanding the acceleration process of ions. These particles can provide important information about the most highly accelerated ions. However, a complication arises in the study of charged particles reaching the Earth, and that is the interplanetary magnetic field. The time that charged particles take in their trip from the Sun to the Earth depends on the geometry of magnetic fields in space, which changes from one flare to the next. This variation makes it impossible to determine uniquely when the charged particles were ejected from the Sun, and so the time profile of the charged particles cannot be directly compared with other profiles at different wavelengths, such as the ultraviolet, radio, and hard X-rays. (Let us call them the observation by optical telescopes.)

On the other hand, the time profile of high-energy gamma-rays can be directly compared with the data from optical telescopes, since they are free from the problem inherent to charged particles. The data for solar neutrons can also be compared with that from optical telescopes

if the energies of the neutrons can be measured. Otherwise it would not be possible to determine whether the neutrons are produced instantaneously or continuously at the Sun.

Among the candidates for solar neutron events (Koga et al. 2017), there is an interesting example that was found in the flare observed on 2012 June 3. The event included prominent features, including high-energy ions that were accelerated to a few GeV within about one minute (Share et al. 2018), and also high-energy gamma-rays and neutrons that were produced by interactions with the solar atmosphere. The analysis of data on this event is almost free from inherent problems such as the production time of neutrons.

Figure 1 shows a prominent feature of the flare observed by the GOES satellite which shows that the flare continued for only about one minute.¹ The flare was located at the solar coordinates N16°E33° and the Earth was 46.1° above the solar horizon. Fortunately, the event was also observed by the Reuven Ramaty High Energy Solar Spectroscopic Imager (RHESSI) and Gamma-ray Burst Monitor onboard the FERMI satellite (FERMI-GBM) (Meegan et al. 2009). Figures 2 and 3 present the data for the hard X-ray region.

A preliminary report on this event was presented at the 35th International Conference on Cosmic Rays (Kamiya et al. 2017). Following the conference, the authors ran Monte Carlo simulations of various interaction processes between accelerated ions and the solar atmosphere, and studied whether the observed results could be reasonably explained by the results of simulations which took several magnetic field patterns into account. The GEANT4 code was used as the basis for the simulations and will be summarized later in this work.

The paper is comprised as follows. Section 2 describes how to extract neutron signals from the raw data, then section 3 introduces the flux of gamma-rays and neutrons observed in the flare on 2012 June 3 and compares the intensities at the top of the atmosphere as measured by the FERMI-LAT (Large Area Telescope) and SEDA-FIB (Space Environment Data Acquisition system by the FIBer type detector) instruments. Section 4 presents the results of the Monte Carlo simulation and examines whether they explain the observations. Section 5 presents the prediction by the Monte Carlo simulation under a converging magnetic field. Section 6 compares the results for this flare with those of other events, and section 7 discusses possible ion acceleration processes for the flare on 2012 June 3. Section 8 is a summary and presents the conclusions drawn from the results.

¹ See (<ftp://ftp.swpc.noaa.gov/pub/warehouse/2012>).

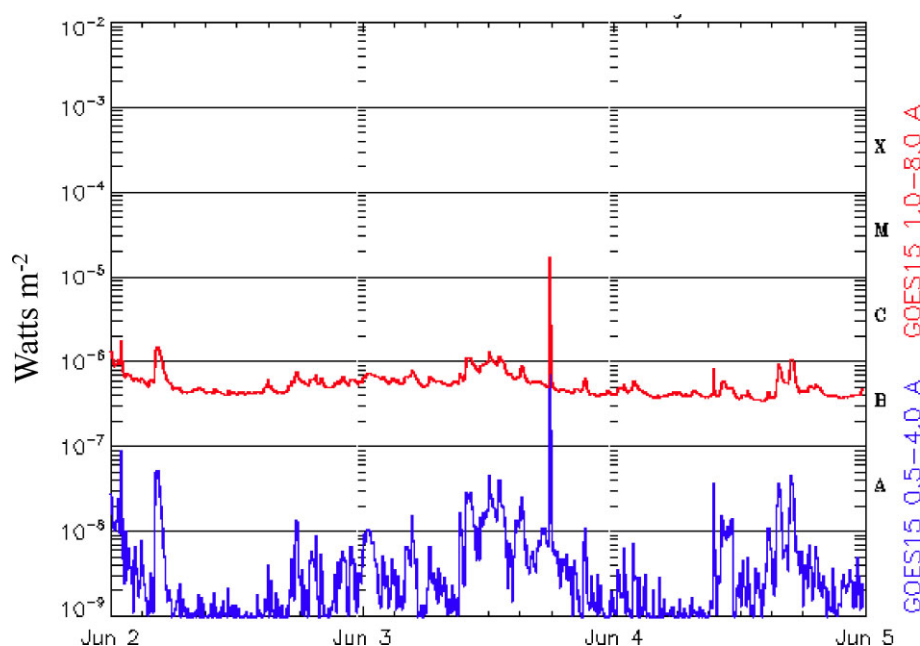


Fig. 1. Time profile of GOES soft X-rays on 2012 June 3. A sharp peak can be recognized around at 17:53 UT. The red curve (upper curve) corresponds to X-rays emitted in the band of 1–8 Å; the blue plot (lower plot) represents the X-ray intensity in the band of 0.5–4 Å. The vertical axis represents W m^{-2} . (Color online)

2 How to find solar neutrons with the SEDA-FIB

2.1 Detecting solar neutrons with the SEDA-FIB

This section describes the method for detecting solar neutrons using the SEDA-FIB. For studying solar neutrons, the authors have prepared a new type of detector that not only = determines the neutrons' trajectories but also measures the deposited energies along the tracks (Koga et al. 2011; Muraki et al. 2012). The detector was installed on the International Space Station (ISS), where it operated between 2009 August 25 and 2018 March 31.

The ISS passes over the daylight part of the Earth for 60 minutes, then passes over the dark night portion for 30 minutes. At any given time, the ISS returns to nearly the same position over the Earth as it occupied 23 hours earlier. Of course, solar neutrons cannot be observed while the ISS is over the Earth's far side from the Sun so, because of this, and the fact that both the ISS and the FERMI satellite orbit the Earth in 92.5 minutes, simultaneous observations of gamma-rays and neutrons from the sun do not occur often.

Figure 4 shows the principle of the SEDA-FIB detector. When a high-energy neutron enters the plastic scintillator block and causes a nuclear interaction via the charge-exchange process between the nuclei in the scintillator, the neutron is converted into a high-energy proton and continues forward. The opening angle θ between the paths of the neutron and the proton is as shown in figure 4, and the incident energy of the neutron (T_n) can be uniquely

expressed as $T_n = T_p / \cos^2 \theta$ using the measured proton energy (T_p). This applies when neutrons collide with the proton target inside the scintillator. When a neutron collides with a carbon target, only the lower limit of the incident energy of the neutron can be determined, so the incident neutrons have a higher energy than what was observed.

Neutron-produced protons traveling through the scintillator lose energy when they cause ionization and can stop altogether in the scintillator, but many of the more-energetic protons induced by neutrons inside the scintillator block penetrate and emerge from the block ($E_p > 120$ MeV). Such a signal is then rejected by an anti-counter surrounding the cubic scintillator block. The anti-counter consists of six layers of plastic scintillator material with a thickness of 1 cm and covering an area of $10 \times 10 \text{ cm}^2$, and its signals are independently sensed by six photomultipliers. The anti-counter system is unable to determine whether the charged particles came from outside or were produced inside the scintillator.

The sensor is located in the center of the detector and consists of a small piece of tubular scintillation fiber that is 6 mm wide, 3 mm high, and 96 mm long. Sixteen scintillation tubes are attached to each other edge to edge, forming a plane 3 mm thick. Let us call this plane the X layer. An identical layer, the Y layer, is stacked on top of it to form a rectangular angle. In this fashion, 16 X layers and 16 Y layers are arranged alternatively to make a sensor that can measure the arrival direction of neutrons.

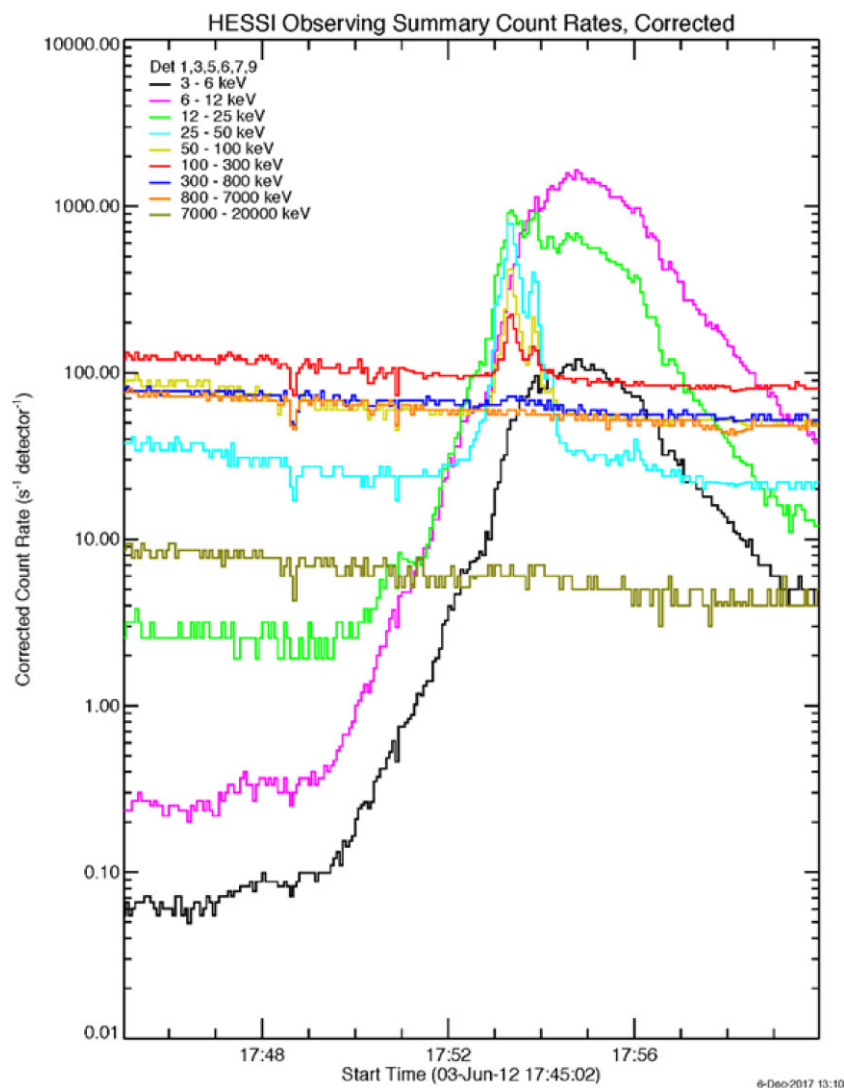


Fig. 2. Time profile around 17:53 UT observed by the RHESSI satellite. The red curve indicates the time profile of X-rays in the energy band of 100–300 keV. The soft X-rays (black, magenta, green) were emitted for a slightly longer time compared with the hard X-rays. (Color online)

When a neutron-produced proton arrives, its track must run through at least two X layers and two Y layers for its direction to be determined. This limits detection to protons with energies above 35 MeV and sets the threshold energy of the detector to ≥ 35 MeV. With the stated upper limit of high-energy protons, this gives the detector a range of 35 to 120 MeV for finding solar neutron-produced protons with the SEDA-FIB.

The signals from the scintillation tube reach the surface of the 256 channel multi-anode photomultiplier (MAPMT, Hamamatsu H4140-20) via an optical fiber 1.5 mm in diameter. The light intensity from the track is converted to a digital representation and the number is moved to storage in the Space Environment Data Acquisition (SEDA) system. The accumulated data is transmitted periodically to the ground stations and then to the Kibo control room at the Tsukuba Space Center.

Solar neutrons with an energy of 35 MeV arrive at Earth 22 minutes after light that left the Sun at the same time. During these 22 minutes after the peak of hard X-rays, solar neutron data is analyzed. The sensor's detection efficiency has been evaluated by Monte Carlo simulation, and was found to depend slightly on the incident energy of neutrons and to be roughly constant at 0.020 ± 0.002 ($\sim 2\%$) (Muraki et al. 2016). These values are used when the flux of neutrons arriving at the top of the atmosphere is converted.

2.2 Actual process of the data analysis

The direction of the Sun is used for reducing the background from the data stream. Information on the solar direction was provided by the sensor of the all-sky X-ray monitor attached to the MAXI detector, another sensor that is mounted on the Japanese Experiment Module (JEM) on

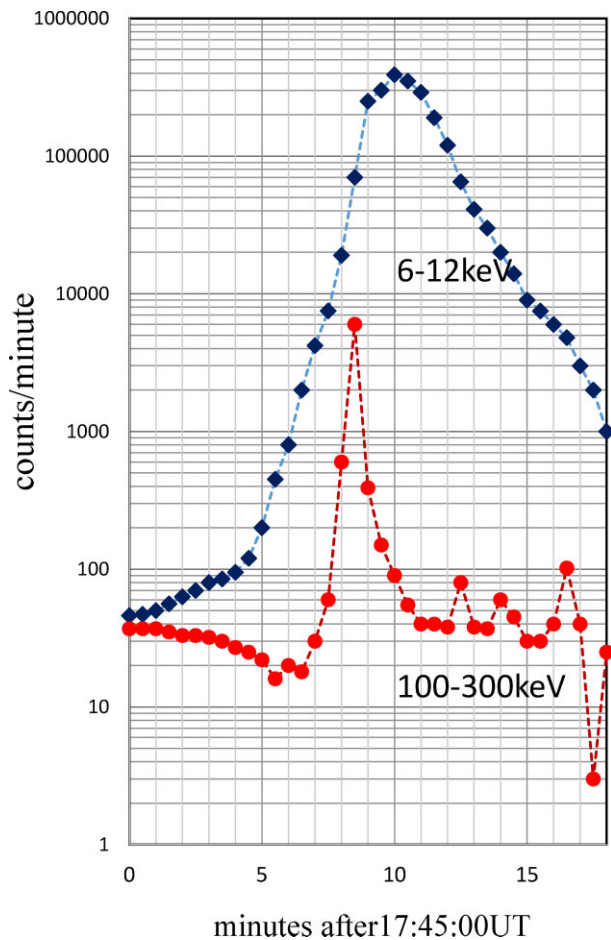


Fig. 3. Same time profile of hard X-rays around 17:53 UT observed by the FERMI-GBM NaI/CsI counters. The red color plot (solid circle) indicates the time profile of hard X-rays detected in the energy band of 100–300 keV; the blue color plot (diamond) indicates the time profile observed in the soft X-ray region (6–12 keV). The excess of hard X-rays continued only for a few minutes. The vertical and horizontal values represent count per minute and minutes after 17:45:00 UT, respectively. The original plot is available from the website of the FERMI-GBM team (The RHESSI Browser).² (Color online)

the ISS. Protons emitted inside a solid angle of 45° centered on the Sun were selected as candidate as solar neutrons. The choice of 45° was determined from the results of the Monte Carlo simulation shown in figure 5 (Muraki et al. 2013). Figure 5 tells us that 95% of neutrons with the energy 60 MeV are involved in the data analysis by this criterion.

A “directional cut” of the tracks was chosen in deciding the reduction of the background noise. Suppose the background is coming into the detector in an isotropic way. The selection of the particles entering into the cone with an opening angle of 45° will then reduce the background down to $\sim 1/7$, because the solid angle of the cone with an opening angle of 45° is estimated as 0.58π steradian. We have made a numerical calculation to determine the

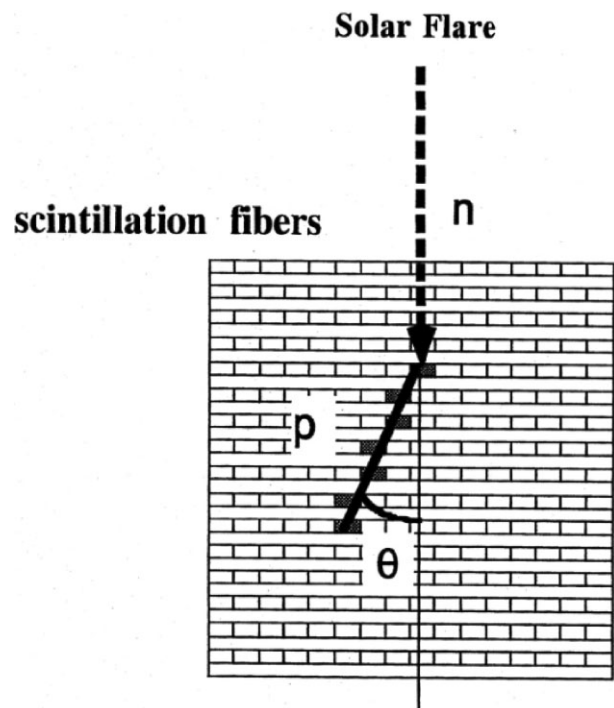


Fig. 4. Schematic diagram of the detection principle of solar neutrons by SEDA-FIB. A high-energy neutron enters in the plastic scintillator fiber block and produces a high-energy proton by the charge exchange process. The six surfaces of the central scintillator block are surrounded by the anti-counter. The anti-counter is used for the rejection of charged particles.

acceptance of the sensor as a function of the solar direction to the x – y plane. Between 17:53 and 18:13 UT, the solar direction was almost vertical to the x – y plane (parallel to the z -axis). The acceptance weakly depends on the solar direction, which was $(98 \pm 2) \text{ cm}^2$ for the entrance of solar neutrons.

Next we test the possibility of using actual data to determine how the background is actually reduced by applying the directional cut. Figure 6 shows the trajectory of the ISS in orbit at 16:00 UT and 19:30 UT on 2012 June 3. The blue part of the trajectory corresponds to night time on Earth, whereas the red part corresponds to daytime.

Figure 7 shows the counting rate of the SEDA-FIB detector at 15:00–19:30 UT on 2012 June 3 with the horizontal axis in units of minutes. The impulsive flare was detected around 17:55 UT, as indicated by the green arrow in the figure. The box denotes the counting rate of the SEDA-FIB, whereas the red circle denotes the event rate after applying the directional cut to extract solar neutrons. In the figure, a no-detection point (the zero point) is shown by an open circle. These points line up on the horizontal axis. The South Atlantic Anomaly (SAA) region is indicated by the horizontal red bars in the figure. Because the counting rate near the SAA region increased to more than 10 times in comparison with the normal path, the data were

² (<http://sprg.ssl.berkeley.edu/~tohban/browser/?show=grth+qlpcr>).

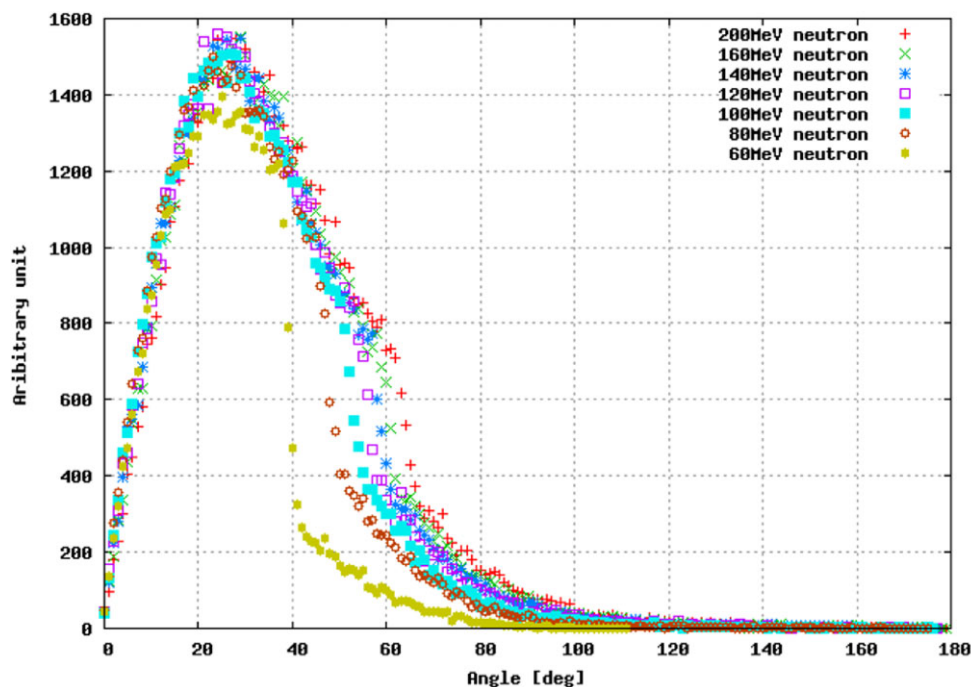


Fig. 5. Angular distribution of the emitted protons by the collision between the incident neutron and the nucleus in the plastic scintillator. From top to bottom, the incident energy of neutrons is 200, 160, 140, 120, 100, 80, and 60 MeV, respectively. The detection threshold is set at >35 MeV and the trigger condition has been included in the Monte Carlo simulation. As the simulation code, the GEANT4 program was used. (Color online)

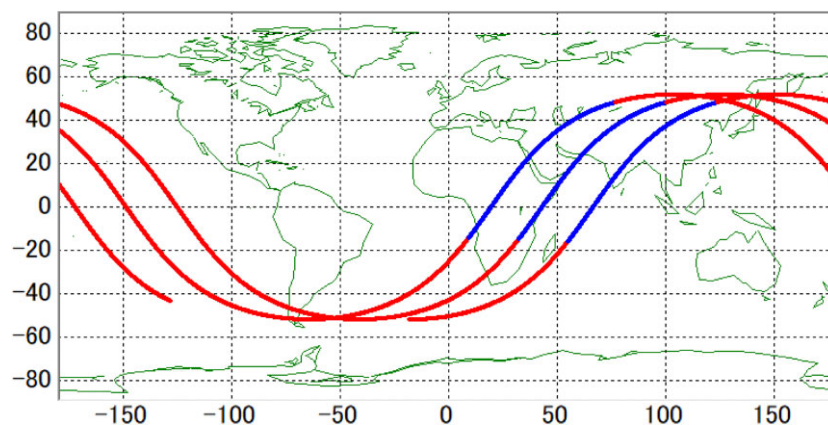


Fig. 6. Trajectory of ISS of three orbits from 15:00 to 19:30 UT is shown. The blue part of the trajectory corresponds to the night region and the red part to daytime of the Earth. (Color online)

not used for the present analysis. Nighttime for the ISS is shown by the black bar under the horizontal axis.

The solar neutron flux may be reproduced after subtracting the background. To estimate the background rate precisely, the authors applied a “superposed” background method. The superposed background was created by using the three different tracks when the ISS occupied nearly the same trajectory as at 17:48–18:12 UT on 2012 June 3 in the flare time. The track on 2012 June 3 is shown in figure 8a. The star on the track corresponds to the time when the impulsive flare reached its maximum intensity, at 17:55 UT. The background was estimated, having superposed the

three-day event rates recorded during 19:31–19:55 UT on June 1, 18:40–19:04 UT on June 2, and 16:49–17:13 UT on June 4. From the superposed background, the neutrons coming from the solar direction were selected. In order to compare them with the one-day data of June 3, the events from the solar direction in the superposed background were normalized, dividing the sum data by a factor of 3. The normalized background from the solar direction is plotted by the triangle in figure 8b. On the other hand, the three-day-averaged background is indicated by the box in figure 8b.

The event rate coming from the solar direction on 2012 June 3 during 17:48 to 18:12 UT is shown by the red circle

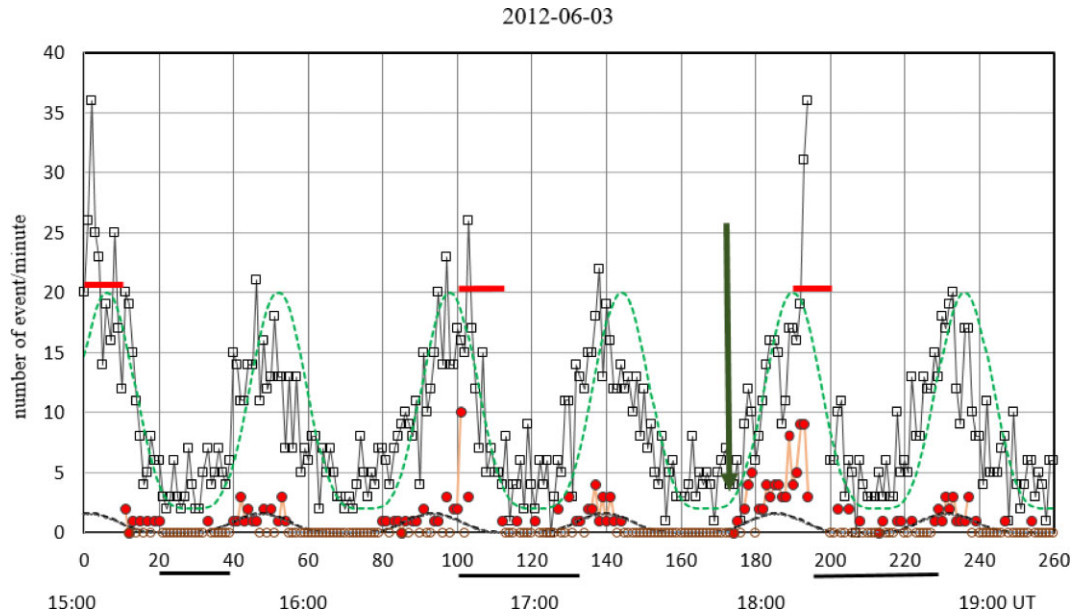


Fig. 7. Counting rates of the SEDA-FIB between 15:00 and 19:30 UT on 2012 June 3 are presented by the following symbols: box (\square) = total counting rate, red circle (\bullet) = tracks coming from solar direction, open circle (\circ) = no-detection point (the zero point), red line (—) = SAA region, black line (—) = night time, and green arrow (\downarrow) = flare start time. The green and black dashed curve under part represent the empirical curve of $A \sin^4[\pi(t-t_0)/T]$. The parameters A and t_0 are given in the main text. T is taken as 46 minutes. (Color online)

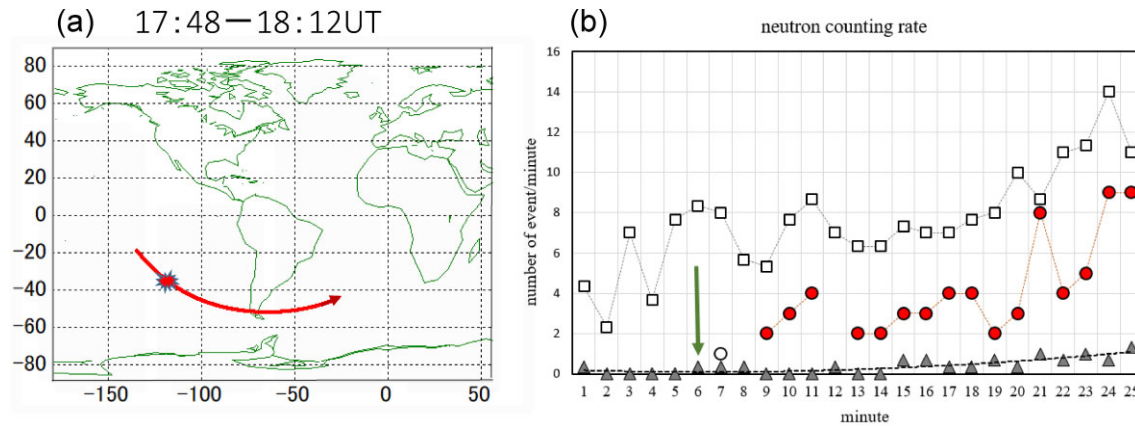


Fig. 8. (a) Trajectory of the ISS between 17:48 and 18:12 UT on 2012 June 3. The star on the trajectory shows the position when the impulsive flare occurred. (b) Superposed background event rate on June 1, 2, and 4 is shown by the box (\square), when the ISS passed the same trajectory of the flight on 2012 June 3 during 17:48 and 18:12 UT (the flare time). The averaged event rate coming from the solar direction in the time of no flare day (June 1, 2, and 4) is presented by the triangle (\blacktriangle). The value is normalized to one day rate (divided by 3). The red filled circle (\bullet) represents the neutron event rate coming from the solar direction on 2012 June 3. When we compare the red filled circles (\bullet) with the grey triangles (\blacktriangle), a clear excess after 17:56 UT of the red circles over the grey triangle (background) can be recognized. The superposed and averaged event rates (\square , \blacktriangle) of the vertical number represent the average background counting rate and the background arriving from the solar direction. We present the data point at 17:54 UT (horizontal column 7) by the open black circle, since the point is consistent with the background. The peak time of gamma-rays of FERMI-LAT is shown by the green arrow. (Color online)

in figure 8b. When we compare the red circles with the grey triangles, the excess of the flare time on June 3 is apparent. They are arriving from the solar direction after the impulsive flare.

A few notes are added here. The red circles of figure 8b did not involve the gamma-ray events. They were already removed from the data points of figure 8b by checking the ionization loss of the track deposited in the scintillation

tube. Furthermore, there is an open circle at 17:54 UT (at the seventh column on the horizontal axis). The data point may be consistent with the background. Therefore, we did not use this data point in the analysis.

Candidate neutron events arriving from the solar direction are shown by red circles in figure 7, while the trigger rate is shown by the box. The curves were empirically fitted by applying the function of

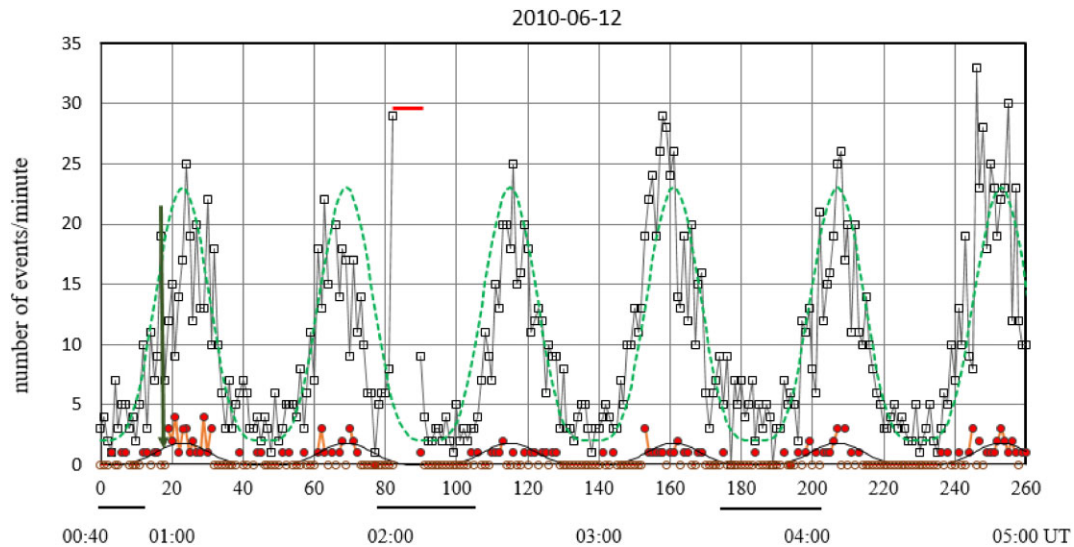


Fig. 9. Same plot as figure 7 but for the SOL2010-06-12 event. The counting rate of SEDA-FIB during 00:40 and 05:00 UT is shown. The peak intensity of the hard X-rays was observed at 00:55:30 UT. The vertical green arrow indicates the peak time. (Color online)

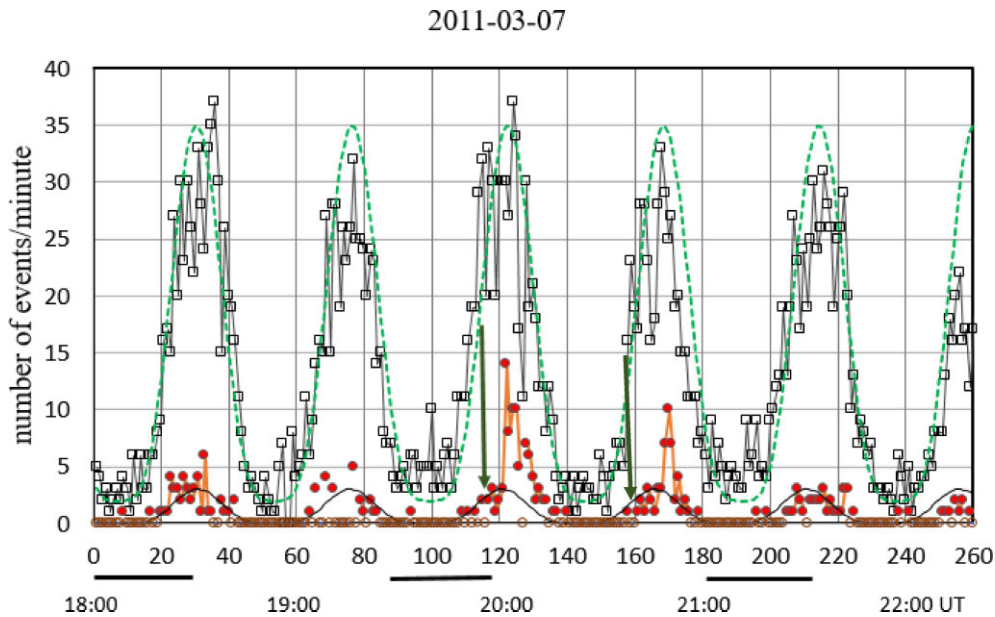


Fig. 10. Time profile of SEDA-FIB for the SOL2011-03-07 event. The same plot as figures 7 and 9, but for the time from 18:00 to 22:30 UT on 2011 March 7. The peak intensity of hard X-rays was observed twice, at 19:58 UT and 20:37 UT. The vertical green arrows represents these times. A_1 and A_2 are estimated as 35 ± 7 and 3.0 ± 1.2 (events per minute), respectively. (Color online)

$A \cdot \{\sin[\pi(t-t_0)/T]\}^4 + C$ to these points. The green dashed curve represents the smoothed trigger rate, while the black dashed curve corresponds to the events arriving from the solar direction. The parameters A and t_0 for the trigger rate are $A = 18$, $t_0 = 29$, and $C = 2$, while for the events coming from the solar direction, the parameters are expressed as $A = 1.6$, $t_0 = 24.5$, and $C = 0$. Here T was taken as $T = 46$ [min]. The events shown by red circles involve gamma-ray candidates.

When comparing the two factors of A for each series of events (without directional cut and with directional cut),

it is possible to recognize that the background has been reduced by a factor of about 12 by the directional cut. After 17:56 UT (at the point of column 9 or 17:56 UT) in figure 8b the neutron event rate (red circle) of June 3 clearly exceeds the background (triangle). The statistical significance of the event has been estimated as 4.3σ for the events between 17:56 and 18:06 UT (from the ninth to the 19th point) and 7.2σ to the events between 17:56 UT and 18:12 UT (from the ninth to the 25th point). The statistical significance has been derived by the conservative Li–Ma method (Li & Ma 1983).

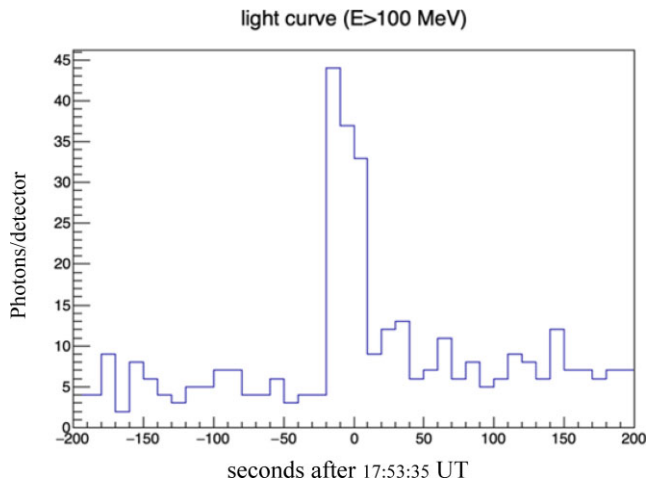


Fig. 11. Time profile of high-energy gamma-rays with energy higher than $E_\gamma > 100$ MeV observed by the FERMI-LAT. The origin of the horizontal axis is set at 17:53:35 UT. The 10 s value is plotted. The light curve is created based on the LAT low energy data (LLE). After the very impulsive production of gamma-rays, a weak emission of high-energy gamma-rays continued for 8 min. (Color online)

Before determining the differential energy spectrum of solar neutrons in the above events, let us show the data for other events. Figures 9 and 10 present the time profiles of the events observed in SOL2010-06-12 and SOL2011-03-07 (Muraki et al. 2020). The peak time of the impulsive flare is shown by the green arrow in each figure. The detailed discussions on these events will be provided in the later sections.

3 Observed fluxes of high-energy gamma-rays and neutrons

This section compares the flux of neutrons ($E_n > 35$ MeV) to that of gamma-rays ($E_\gamma > 100$ MeV) that were measured by the SEDA-FIB and FERMI-LAT instruments, respectively.

3.1 Detecting gamma-rays with the LAT detector

Figure 11 presents the time profile of high-energy gamma-rays detected by the FERMI-LAT. The data show that most of the excess of gamma-rays continued for one minute only, with the peak time being 17:53:35 UT. Figure 12 shows the energy spectrum (Kamiya et al. 2017). The energy spectrum of gamma-rays can be fitted with power spectrum $E^{-\gamma}$ with an index $\gamma = (2.7 + 0.9 - 0.2)$. There are no high-energy photons beyond 600 MeV, so the maximum energies of accelerated ions in this flare may be limited to a few GeV per nucleon. The number of photons between 17:53:15 and 17:53:45 UT was 101 ± 10 .

The effective area of the LAT at 17:53:15 UT is estimated to be $\approx 2000 \text{ cm}^2$ for a polar angle of 30° at $E_\gamma \approx 125$ MeV.

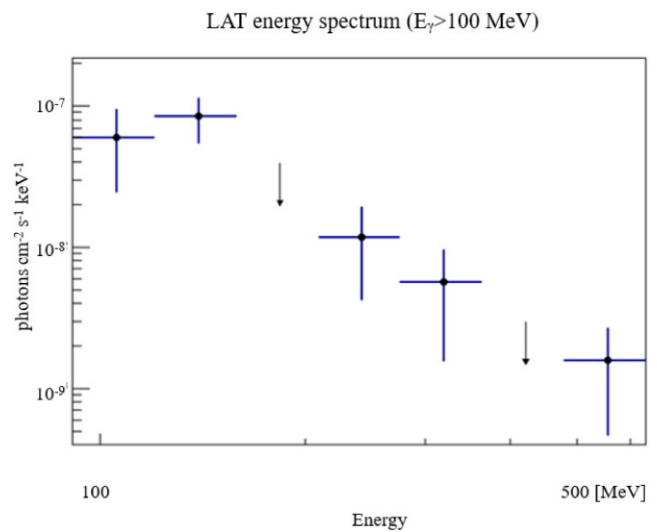


Fig. 12. Energy spectrum of high-energy gamma-rays. No high-energy gamma-ray was detected beyond 600 MeV. The vertical axis is presented in the units of $[\text{photon cm}^{-2} \text{ s}^{-1} \text{ keV}^{-1}]$. The vertical arrow depicts the 95% upper limit of the flux at the corresponding energy bin after the reduction of the background. By taking into account the error bars, the differential energy spectrum of gamma-rays in the region of $E_\gamma = 120$ –600 MeV may be approximately presented by a power law of $E_\gamma^{-\Gamma} dE_\gamma$, where Γ is given by $\Gamma = 2.7 + 0.9 - 0.2$. (Color online)

The Fermi satellite was flying over the west coast of Mexico (116.2°W , 8.54°N) then, and the local time was 10:10 a.m. The opening angle between the sun and the vertical axis of the LAT was estimated at 30.1° . Therefore, the number of events (101) is converted into the number per unit area, which turns out to be $\approx 0.051 \pm 0.005 \text{ photons cm}^{-2}$.

3.2 Detection of solar neutrons with the SEDA detector

Before comparing the flux of gamma-rays with that of solar neutrons, we will briefly explain in this section how solar neutron events were selected. First the directional information of the track was used, as provided by the SEDA-FIB. Tracks within 45° of the Sun were selected as the candidates for solar neutrons. As shown in figure 7, the directional information reduces the background to less than $1/12$. Around 17:42 UT, the ISS flew over the equator when the minimum background was observed as $\approx 0.2 \text{ count min}^{-1}$. Between 17:53:15 and 18:13:00 UT, there were 71 solar neutron candidates. From this the possible entrance of about four gamma-rays were removed. The direction of the Sun was opposite the main background source of the ISS. Therefore, the separation of signal and background was rather easily made. Figure 13a shows the angular distribution of 67 neutron events coming from the solar direction, and figures 13b and 13c present the angular distribution of

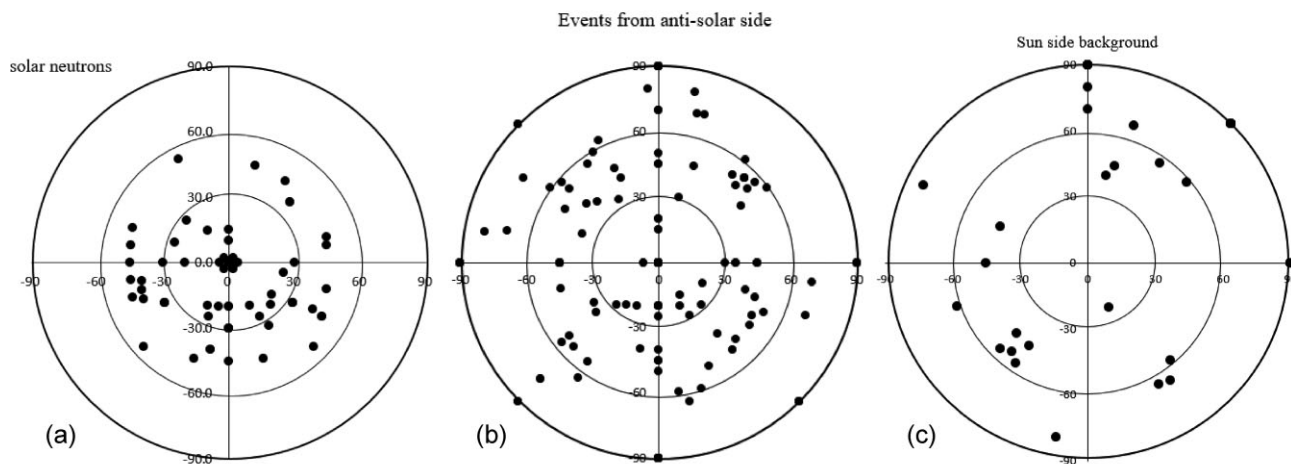


Fig. 13. (a) Angular distribution of protons emitted by solar neutrons. The center corresponds to the solar direction. (b) Arrival direction of all incident particles during 17:48 and 18:13 UT is presented on the polar coordinate. The center looks anti-solar direction within $\pm 10^\circ$ during the time. (c) Angular distribution of the tracks entering into the surface looking the solar direction. The candidates of solar neutrons were removed and the center corresponds to the solar direction within $\pm 10^\circ$ during the time.

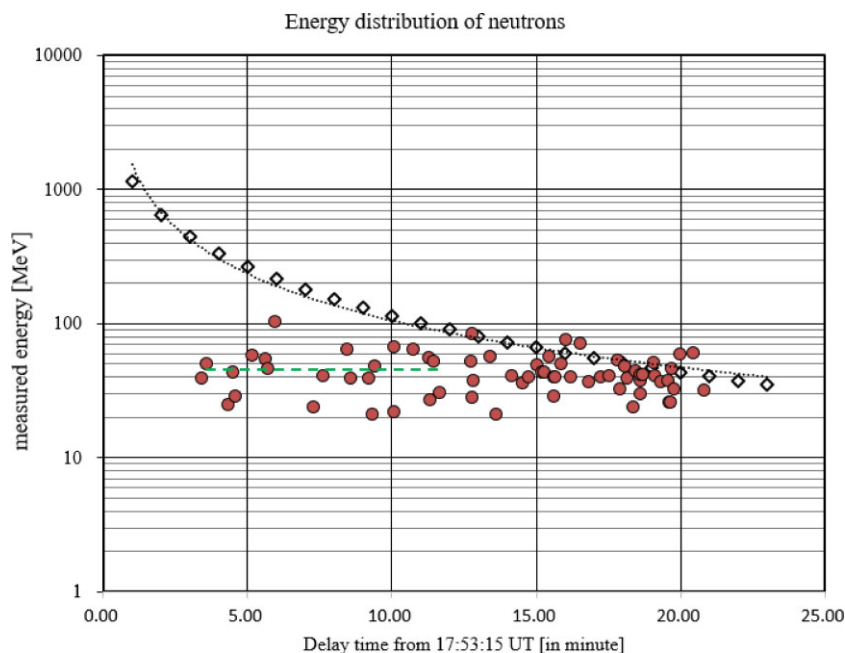


Fig. 14. Energy distribution of protons recorded by the sensor of SEDA is shown as a function of the elapsed time from the peak time of the flare; 17:53:15 UT in the unit of minutes. The dotted curve with a diamond (\diamond) represents the expected arrival time of neutrons with the energy in the case of an impulsive flare. The number for the vertical energy corresponds to the energy of neutrons, while for neutron-produced protons (circle, \bullet) the value corresponds to the energy of protons. The SEDA sensor cannot record high-energy protons over 120 MeV, as indicated by the green dashed line. The event threshold is set at about >35 MeV. (Color online)

all arrival background from the anti-solar and solar directions, respectively. The solar neutron candidates have been removed from figure 13c. Assuming that these neutrons were emitted instantaneously at 17:53:15 UT, the energy spectrum was derived from the flight time. Even assuming that the production time was 17:53:35 UT, the effect on the power index was less than 0.1.

Before we derive the energy spectrum of solar neutrons by the time of flight method, we examine the accuracy of the time of flight method. The dashed line with the open diamond in figure 14 presents the expected arrival time distribution of solar neutrons by the time of flight, while the red circles represent the arrival time of each event with the energy measured by the range method (by measuring the

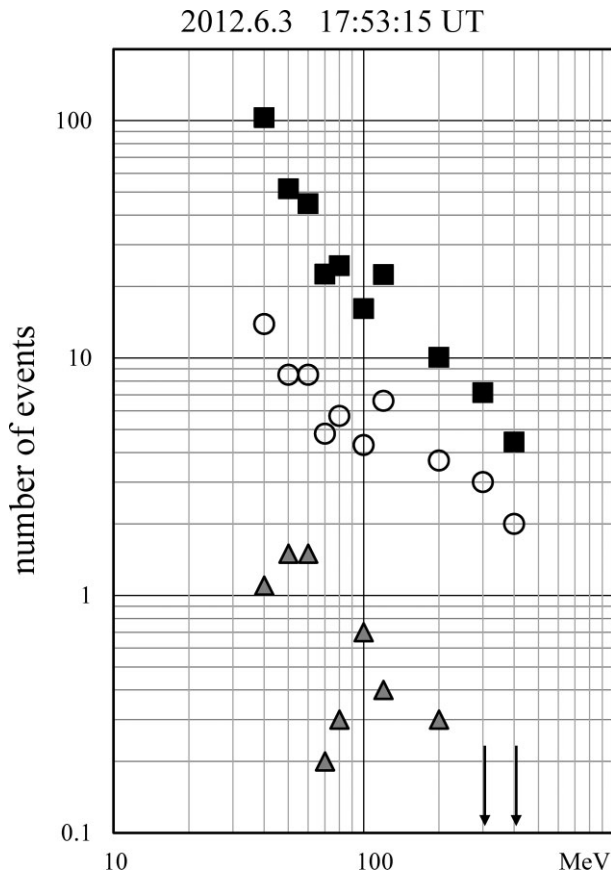


Fig. 15. Energy spectrum of solar neutrons, assuming an instantaneous production at 17:53:15 UT. The energy of each neutron was determined by the flight time, assuming an instantaneous production of neutrons 20 s before the peak time of FERMI-LAT gamma-rays with energy of $E_\gamma > 100$ MeV. The background and raw data are shown by the triangle (\blacktriangle) and the circle (\circ) respectively. The decay corrected data to the solar neutron component is presented by the box (\blacksquare).

track length). As already described before, high-energy protons with the energy > 120 MeV could not be detected by the SEDA-FIB. We measured the proton energy by two different methods: the range method and the deposited energy measurement method by the ADC (Analog Digital Converter). The range method is expected to have better energy resolution than the ADC measurement at high energies, therefore in figure 14 we plot only the results measured by the range method. The energy resolution of proton tracks near the threshold energy was about 25%, however beyond 65 MeV the energy resolution was expected to be better than 10% (Imaida et al. 1999).

Next we evaluate the statistical errors associated with the flux. The effective detection area of the SEDA-FIB is estimated as (98 ± 2) cm² and the number of neutrons after correcting for decay time turns out to be 59.2 ± 13.0 events per the area of 98 cm² for neutrons of $E_n \geq 100$ MeV. The above value includes about 22% statistical errors. This error value stems from the actual event number recorded in

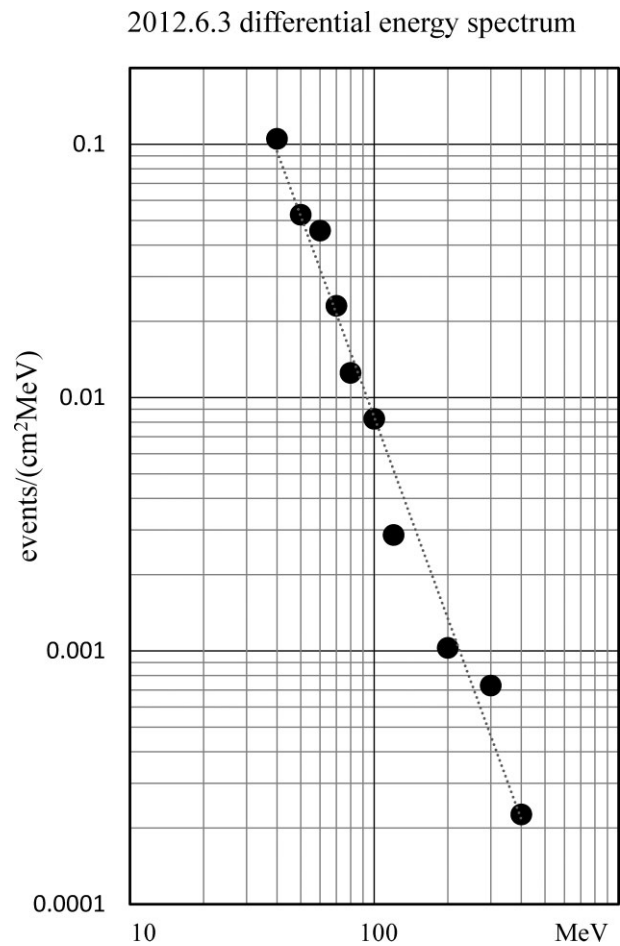


Fig. 16. Differential energy spectrum of solar neutrons observed on 2012 June 3 by the SEDA-FIB detector onboard the ISS (Kamiya et al. 2017). The spectrum may be fitted to a power law with $\gamma = -2.8 \pm 0.3$, indicated by a straight line.

the SEDA FIB detector beyond 100 MeV, i.e., 19.6 ± 4.4 events.

Figure 15 shows the energy spectrum of the raw data (circle) and the decay-corrected data of solar neutrons (box) (Kamiya et al. 2017). The estimated flux of neutrons per unit area is (0.60 ± 0.13) events cm⁻² (for $E_n > 100$ MeV). For those data, a further correction to the detection efficiency of neutrons in the sensor must be made, due to the limited depth of the sensor (10 cm). It is estimated via Monte Carlo simulation to be $2.1 \pm 0.2\%$ (Muraki et al. 2016). Thus, the net intensity of neutrons to be compared to that of gamma-rays is estimated to be (29 ± 6) neutrons cm⁻² for $E_n > 100$ MeV. Based on this value, the neutron flux at the sun was derived as $(6.5 \pm 1.4) \times 10^{27}$ /(sr cm⁻²). This number has been derived by 29 (cm⁻²)/ $\{[1$ cm²/(1.5×10^{13} cm²) sr].

Figure 16 shows the differential energy spectrum of solar neutrons. It was assumed that the neutrons were emitted at the peak time of high-energy gamma-rays, i.e., 17:53:15 UT, and the energy spectrum was obtained by time-of-flight

calculation. The differential energy spectrum is well fitted to a power spectrum with an index $\gamma = 2.8 \pm 0.3$.

Now the fluxes of neutrons and gamma-rays can be compared via the ratio of n and γ . The value of the n/γ ratio is about $(570 + 190 - 160)$ for E_γ and $E_n > 100$ MeV. The ratio was determined from the n and γ flux of (29 ± 6) and (0.051 ± 0.005) , respectively. In what follows, we will examine this high n/γ -ratio in comparison with the results of a Monte Carlo simulation.

4 Comparison of observed results with naïve Monte Carlo calculations

In order to understand the high ratio between high-energy neutrons and high-energy gamma-rays, Monte Carlo simulations were conducted for the collision processes of accelerated ions with the solar atmosphere. These simulations involved both a simple model of the magnetic field of the photosphere and a converging field in the photosphere.

The simulation first created a virtual space extending over 10^7 km² to the horizontal plane. Next, the simulation ran according to the curvature of the solar atmosphere. One million protons and one million helium ions were injected at the center of the plane 3000 km above the solar atmosphere (i.e., above the photosphere), then the angular distributions of high-energy gamma-rays ($E_\gamma > 100$ MeV) and neutrons ($E_n > 35$ MeV) were obtained as a function of incident energies of the protons and helium ions. Because the SEDA-FIB can detect neutrons with energies above 35 MeV, the simulation tracked neutrons with energies down to 30 MeV. For gamma-rays, the simulation allowed for a threshold energy of the FERMI-LAT calorimeter at $E_\gamma > 100$ MeV. According to the instrumentation paper on the FERMI-LAT (Atwood et al. 2009), the threshold energy of the FERMI-LAT calorimeter is ≈ 100 MeV. This threshold energy is determined by the structure of the FERMI-LAT calorimeter.

GEANT4 was used as the simulation code. This code is widely used in high-energy and nuclear physics. First, protons and helium ions were injected vertically to the solar surface without assuming any mirroring effect (i.e., pitch angle $\theta = 0^\circ$). The simulation model of the solar atmosphere provided by Avrett (1981) was used. The energy of protons was changed between $E_p = 100, 200,$ and 500 MeV, and $1, 5, 10, 50,$ and 100 GeV, and the fluxes of secondary particles were estimated for the two cases of solar atmospheric depths, with equivalent gram-forces of 10 g cm⁻² and 50 g cm⁻². The atmospheric depths were $z = 320$ km and 587 km inside the photosphere, respectively. The border between the chromosphere and the photosphere was defined as $z = 0$.

These results can be compared with the pioneering work done by Hua et al. (2002). Figure 17 shows our results. The

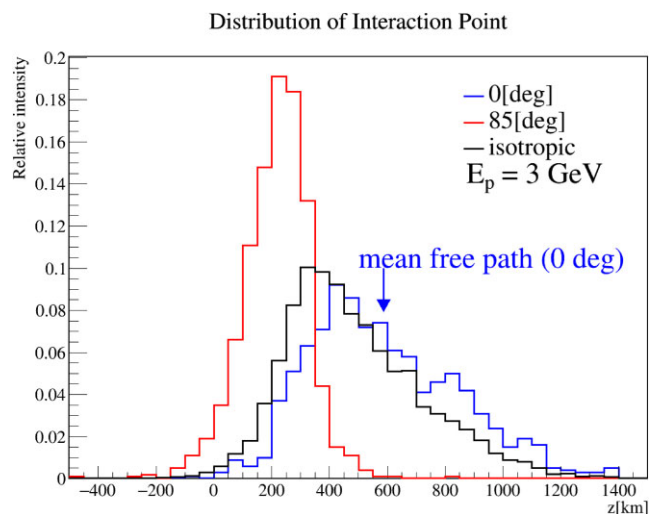


Fig. 17. Interaction point of protons shown as a function of the atmospheric depth of the Sun. The border between the chromosphere and photosphere is taken at $z = 0$. The solid line represents the isotropic entry from $z = -3000$ km in the converging magnetic field. At $z = -3000$ km, the magnetic field strength is set at 10 G. Note that 0° and 85° correspond to the entry of protons with pitch angles of 0° (for vertical entry) and 85° (for almost horizontal entry), respectively. In the case of vertical entry (parallel to the magnetic field), the most probable interaction point is predicted at 25 g cm⁻² or $z = 440$ km. Conversely, in the case of almost horizontal entry (85°), the most probable interaction point is predicted at 5.5 g cm⁻² or $z = 250$ km in the photosphere. (Color online)

black line in figure 17 represents the distribution of interaction points for the isotropic injection of protons with $E_p = 3$ GeV to the solar surface under a converging magnetic field of 100 G. This model of the solar atmosphere and the magnetic field is equivalent to the model used by Hua et al. (2002) (whose results are shown in figure 9 of their paper). The results of Hua et al. indicate that the maximum collision point is located at a slightly deeper region than the border between the chromosphere and the photosphere, which corresponds to $z \approx 200$ km according to this paper's definition. However, present simulation predicts the maximum interaction point at $z \approx 300$ km. The two simulations predict almost the same results. The case of 85° in figure 17 corresponds to where protons were injected almost vertically to the magnetic field line with a peak interaction point of $z \approx 220$ km.

Figure 18 presents the results of the angular distribution of fluxes for each incident energy at a shallow depth of the solar atmosphere (≈ 10 g cm⁻²). As can be seen, the production of secondary particles emitted backwards ($90^\circ - 180^\circ$) is much less than the production emitted forwards ($0^\circ - 40^\circ$). Figures 19 and 20 show the number of secondary high-energy gamma-rays and neutrons within the respective regions of emission angle to the various incident energies of protons. The vertical axis is normalized to the number of “per incident proton” that represents $(1/2\pi \sin\theta)$

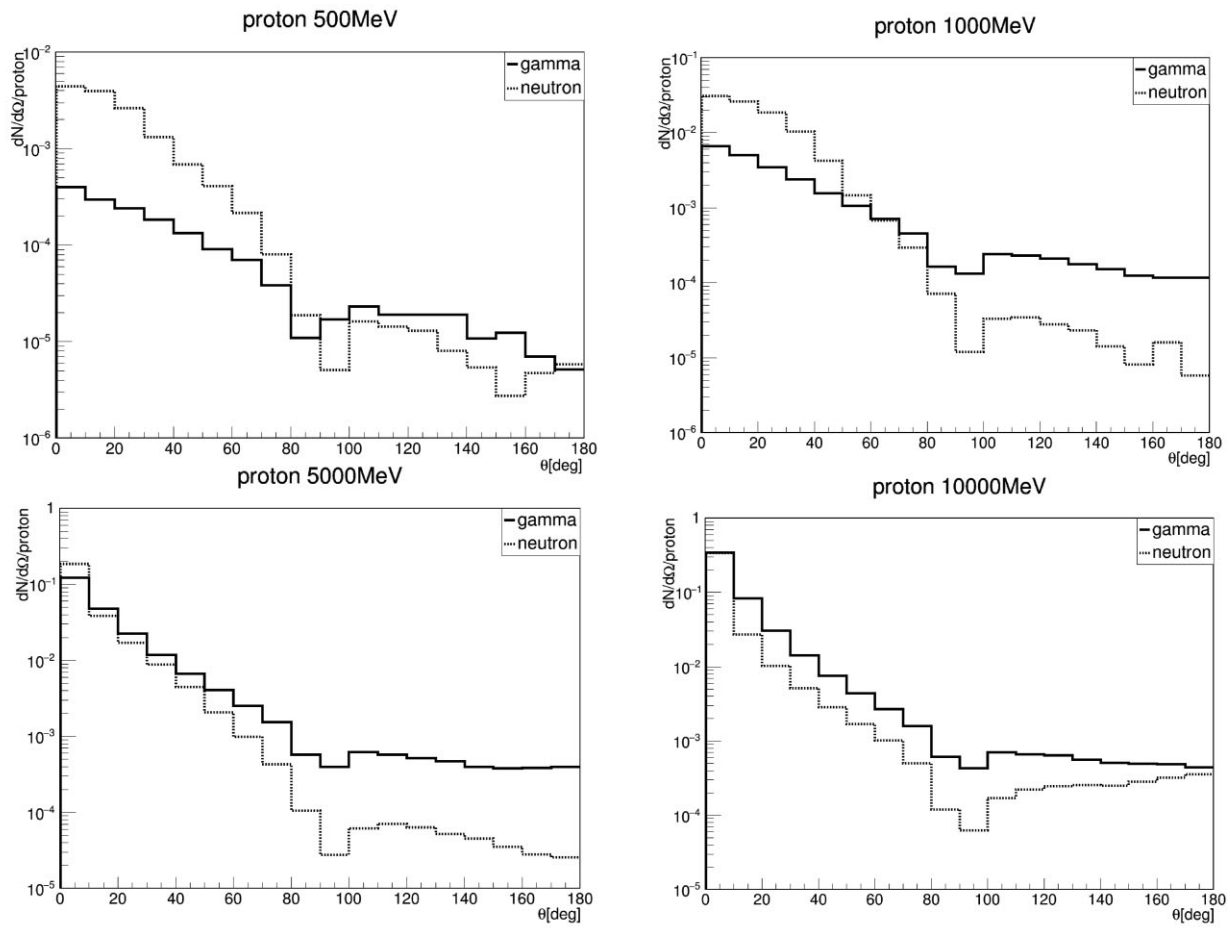


Fig. 18. Angular distribution of neutrons (dotted line) and gamma-rays (solid line). From top left to right and bottom left to right, for protons with energy of $E_p = 500$ MeV, 1 GeV, 5 GeV, and 10 GeV, respectively. When the incident energy increases, the numbers of neutrons and gamma-rays also increase. This is due to the increase of secondary particles with collision energies. The vertical axis is presented using units of $dN/d\Omega$ [events per proton per acceptance]. According to the experimental results of proton–proton collisions at $E_p = 20$ and 100 GeV, the average neutral pion multiplicities are reported as $\langle n_{\pi 0} \rangle \approx 2$ and 3, respectively.

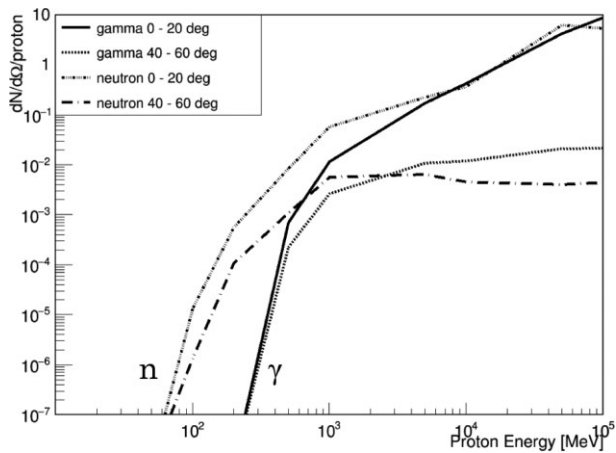


Fig. 19. Flux of neutrons (dash–dotted line and dash–triple–dotted line) and flux of gamma-rays (solid line and dotted line) are presented as a function of incident proton energy for the forward direction ($\theta = 0^\circ - 20^\circ$, $40^\circ - 60^\circ$). The intensity of neutrons generally exceeds that of gamma-rays in an energy range of less than a few GeV than the proton energy (E_p).

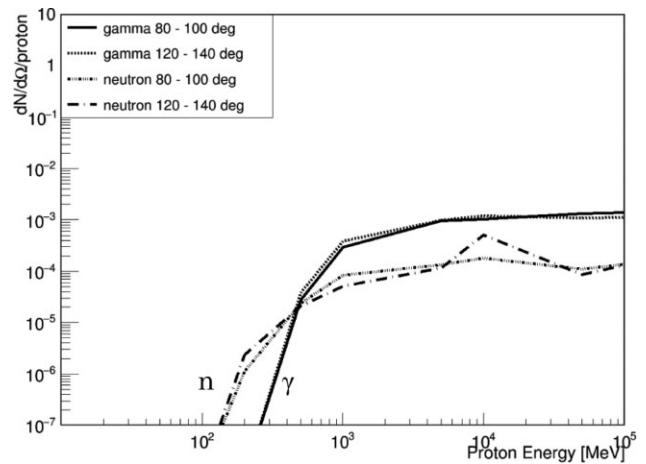


Fig. 20. Flux of neutrons (dash–dotted line and dash–triple–dotted line) and flux of gamma-rays (solid line and dotted line) are presented as a function of incident proton energy for the backward direction ($\theta = 80^\circ - 100^\circ$, $120^\circ - 140^\circ$). The intensity of neutrons is generally lower than that of gamma-rays in an energy range ≈ 400 MeV higher than the proton energy.

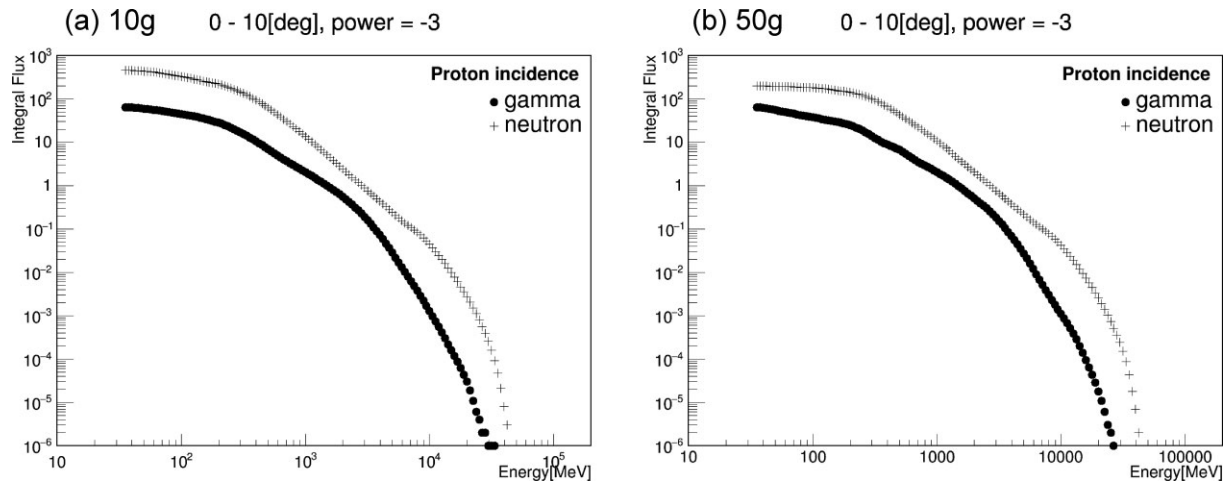


Fig. 21. (a) Integral energy spectrum of neutrons and gamma-rays emitted by the proton incidence in the solar atmosphere of 10 g cm^{-2} thickness (about 320 km inside the photosphere) for the forward direction of $\theta = 0^\circ - 10^\circ$ with power index $\gamma = 3$. (b) Same as panel (a) but for thickness of 50 g cm^{-2} (about 590 km inside the surface of the photosphere).

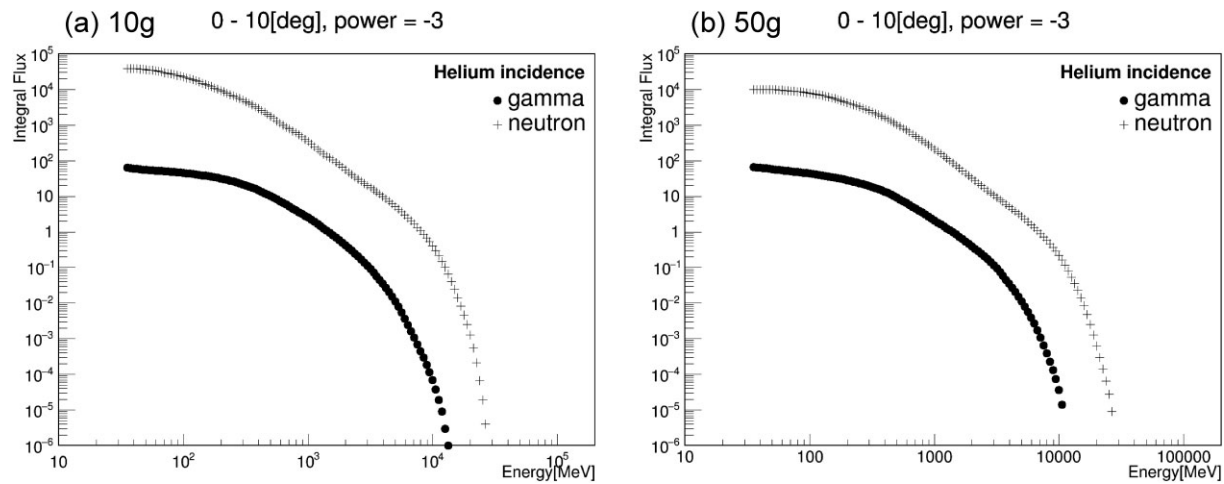


Fig. 22. (a) Integral energy spectrum of neutrons and gamma-rays emitted by the helium incidence in the solar atmosphere of 10 g cm^{-2} thickness for the forward direction of $\theta = 0^\circ - 10^\circ$ with power index $\gamma = -3$. (b) Same as panel (a) but for thickness of 50 g cm^{-2} . Panel (a) predicts that the n/γ -ratio is about ≈ 1000 at E_γ and $E_n \geq 100 \text{ MeV}$.

$dN/d\theta$ or $dN/d\Omega$. The results of the Monte Carlo simulation predict up to about 1000 times more intensive production cross-section in the forward direction ($\theta = 0^\circ - 20^\circ$, $40^\circ - 60^\circ$), as shown in figure 19, than that in the backward direction ($\theta = 80^\circ - 100^\circ$, $120^\circ - 140^\circ$), as shown in figure 20.

In order to compare the results of the Monte Carlo calculation with the observed data, several simulations were run for various cases of proton and helium incidences with different power indices of the energy spectrum from 2 to 7. The fluxes of neutrons and gamma-rays emitted at different emission angles are provided later in figures 34 and 35 for a solar atmosphere of 10 g cm^{-2} with primary power index $\gamma = 3$ of the proton incidence and alpha incidence, respectively.

Figure 21 shows the integral of the energy spectrum of secondary neutrons and gamma-rays emitted in the forward direction of $0^\circ - 10^\circ$ for the proton incidence with $\gamma = 3$, where $\text{Flux}(> E_\gamma) = \int f(E_\gamma) dE_\gamma$ and $\text{Flux}(> E_n) = \int f(E_n) dE_n$. Figure 22 shows the same plot, but for the helium incidence. Similar energy was selected for the helium ions. Here, the collision energy is set for the incident energy per nucleon of the helium nucleus. Figure 21 predicts the n/γ ratio at $E_{n,\gamma} > 100 \text{ MeV}$ as 7.5 for proton incidence. In contrast, figure 22 predicts a much higher n/γ -ratio such as ≈ 1000 for the helium incidence. The results above may provide a possible explanation for the high n/γ -ratio caused by the threshold effect, arising from the difference between proton and helium incidences as described below. As shown in figure 22, the observed high n/γ -ratio suggests that the

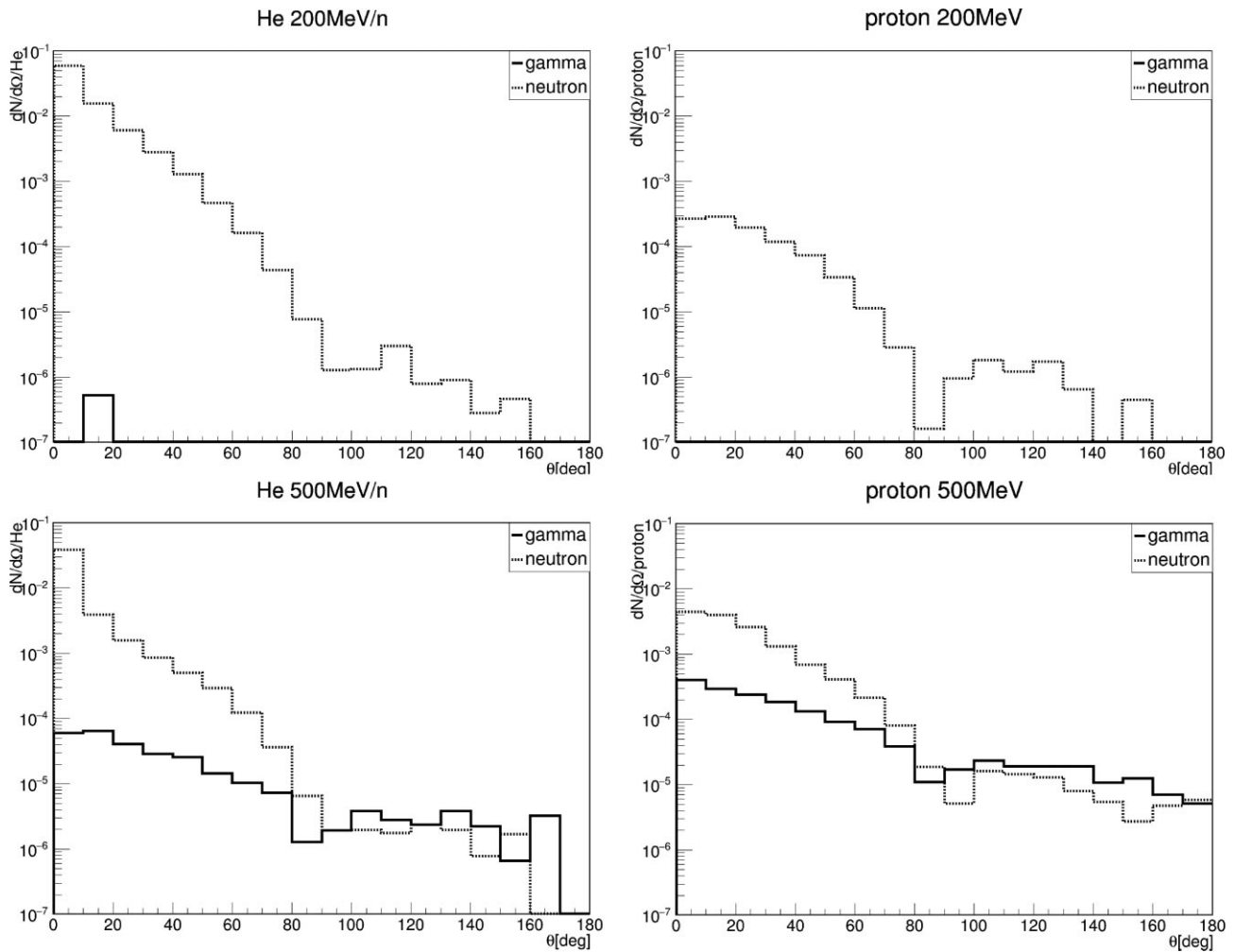


Fig. 23. The threshold effect for the incidence of helium ions is presented together with that of protons for the two incident energies per nucleon. The top panels correspond to 200 MeV nucleon⁻¹, while the bottom panels show slightly higher energies of 500 MeV nucleon⁻¹. Note that the threshold energy of one pion production process is 293 MeV nucleon⁻¹. The dotted line expresses the flux of neutrons, while the solid line represents the photon production. For a comparison, the same scale of helium incidence is used for the vertical scale of proton incidence. Only one photon production is recorded for the helium incidence per the entry of one million helium nuclei in the case of 200 MeV nucleon⁻¹.

dominant acceleration of helium ions may have occurred in the flare on 2012 June 3.

Before closing this section, the threshold effect for the helium incidence needs to be explained. Figure 23 shows how much higher the neutron emission by the helium incidence is in the low-energy region than the proton incidence. The reason is that accelerated helium ions collide with the proton target in the solar atmosphere and the helium nucleus is easily fractured into four nucleons (i.e., two protons, two neutrons). However, for the production of high-energy gamma-rays, the incident energy of protons should exceed $E_p = 293$ MeV because the threshold energy of one pion production process is given simply by kinematics as $E_p = 293$ MeV, and the one-pion production cross-section increases rapidly with the incident energy. Beyond $E_p \approx 600$ MeV, it approaches ≈ 10 mb. The production cross-section of gamma-rays presented in figure 19 suggests this

trend. That is why the threshold effect is predicted for low-energy helium incidence. Given these results, the next section will seek a reasonable acceleration process for ions in order to explain the 2012 June 3 event.

5 Particle production in a magnetic loop on the solar surface and observed results

To understand the actual particle collision and production process by the accelerated ions, the horizontal incidence of primary ions under the magnetic field into the solar surface must be included in the Monte Carlo simulations for forming the fan beam. This may be expected as the accelerated high-energy protons and helium nuclei precipitate over the solar surface trapped by the magnetic loop with the mirroring as depicted in figure 24. When viewed

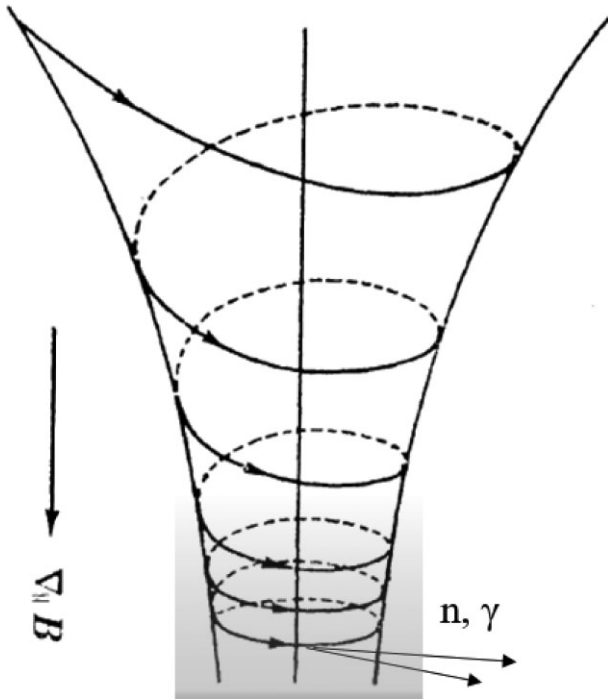


Fig. 24. Drawing: showing the entry of protons and helium nuclei into the solar atmosphere. By the adiabatic invariant of motion, the track is expected to be almost flat relative to the solar surface before mirroring and forming the fan beam; otherwise, protons and helium nuclei will not collide with the solar atmosphere and return in the upward direction.

from the Earth, the secondary neutrons and gamma-rays emitted in the forward direction ($\theta = 0^\circ \sim 40^\circ$) may be preferentially detected. Those secondary particles penetrate the solar atmosphere, emerge from the solar surface, and then arrive at the Earth.

The possibility was already studied by Hua and Lingenfelter (1987), who assumed a highly anisotropic horizontal fan ion beam instead of the isotropic ion beams. A few years later, Hua et al. (2002) conducted a simulation under a converging magnetic field, providing high-energy ions isotopically over the magnetic loop. Through the propagation process, the injected ion beams will form the fan beam naturally at the mirroring point by pitch angle scattering. The converging magnetic field keeps the accelerated ions inside the loss cone and these ions mirror back and forth in the less dense upper solar atmosphere. Such an effect was also included in the present simulation. Following up on such pioneering work, Murphy et al. (2007) investigated the precise relationship that exists between the line gamma-rays and neutrons through simulation. However, their investigation focused on the intensities between the low-energy line gamma-rays and neutrons (Ramaty et al. 1996). Therefore, their results cannot be applied to the present analysis of data observed by the FERMI-LAT (high-energy gamma-rays) and SEDA-FIB, so a new Monte Carlo simulation was needed. For the Monte Carlo simulation, the GEANT 4 program was used under the actual shape of the magnetic field.

Regarding the composition of accelerated ions and following the standard abundance (Reames 1994) in the solar atmosphere, helium ions as well as C, N, O, and Fe ions were included in the Monte Carlo simulation. These ions were injected downward from 3000 km above the photosphere (i.e., $z = -3000$ km). As shown in figure 17, three extreme cases were investigated: two cases of entry at the upper magnetic field with pitch angles of 85° (with ions

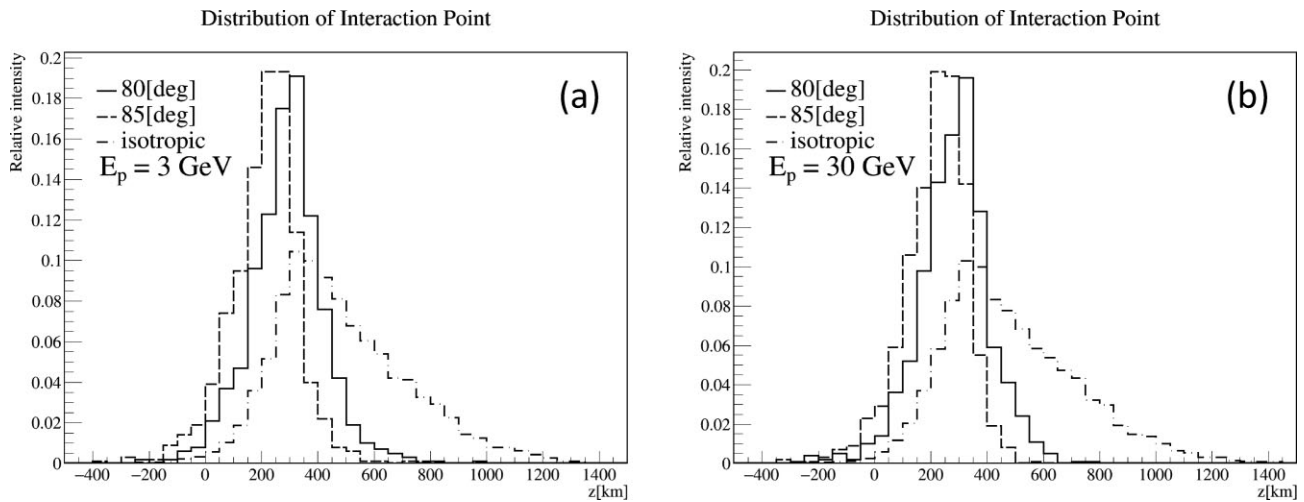


Fig. 25. Distribution of interaction points of the proton beam with the solar atmosphere presented as a function of altitude from the photosphere. The dash-dotted line curve includes the case of the vertical downward beam without a pitch angle, while the solid curve and dashed curve represent the proton beam injected to the solar surface at the top of the solar atmosphere ($z = -3000$ km) with large pitch angles such as 80° and 85° . The dash-dotted line curve shows the case of the isotropic downward proton beam from 3000 km above the photosphere. The initial energy of the proton beam is fixed at 3 GeV (a) and 30 GeV (b), and the magnetic field is fixed at ≈ 100 G. The curvature of the solar surface has been taken into account.

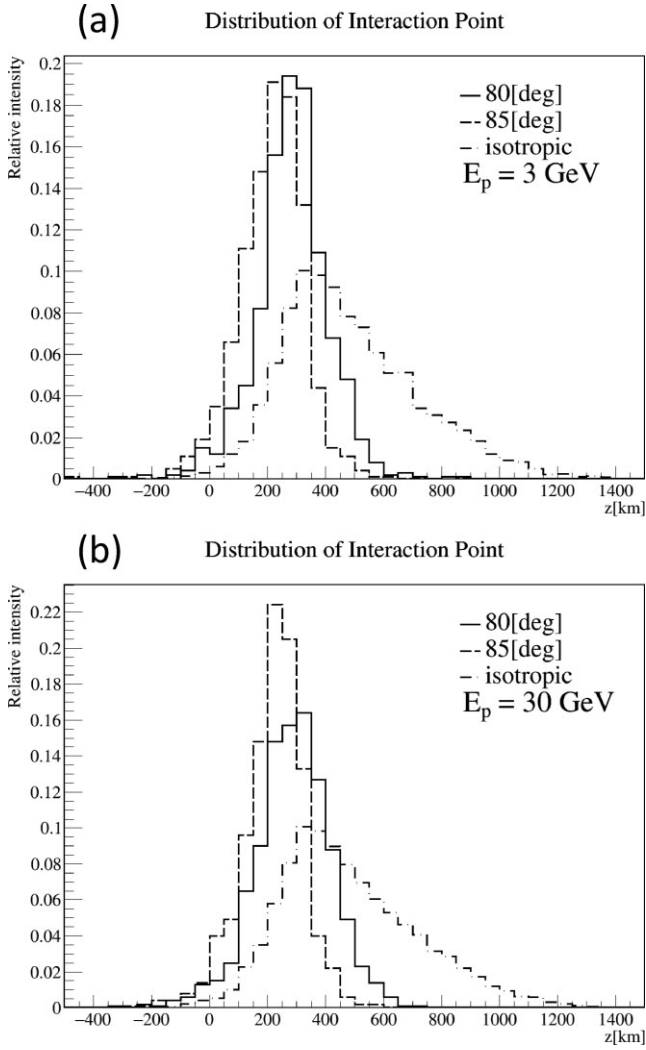


Fig. 26. Same as figure 25, but for a non-uniform converging magnetic field. Details are given in the main text. Proton incidence with energy of (a) 3 GeV and (b) 30 GeV.

being injected nearly horizontally to the magnetic field line) and 0° (with vertical incidence of the ion beam), and one case of the isotropic downward ion beam as investigated by Hua et al. (2002). For a comparison of the results, simulations were done under the uniform magnetic field above the photosphere, assuming field strengths of 10, 100, and 1000 G. Then a more realistic case of a non-uniform converging magnetic field was simulated. (The converging magnetic field was assumed to be $B(z) = (33/100)z + 1000$ [G] in the deep region of $z \geq -3000$ km, while in the upper region of $z < -3000$ km, $B(z)$ was set at the constant value of 10 G; z implies the distance from the photosphere in km.)

Zweibel and Harber (1983) once proposed a model of the solar magnetic field near, but above, the photosphere. According to them, the magnetic field is related with the atmospheric pressure as $B(z)/B(0) = [P(z)/P(0)]^\alpha$. In the

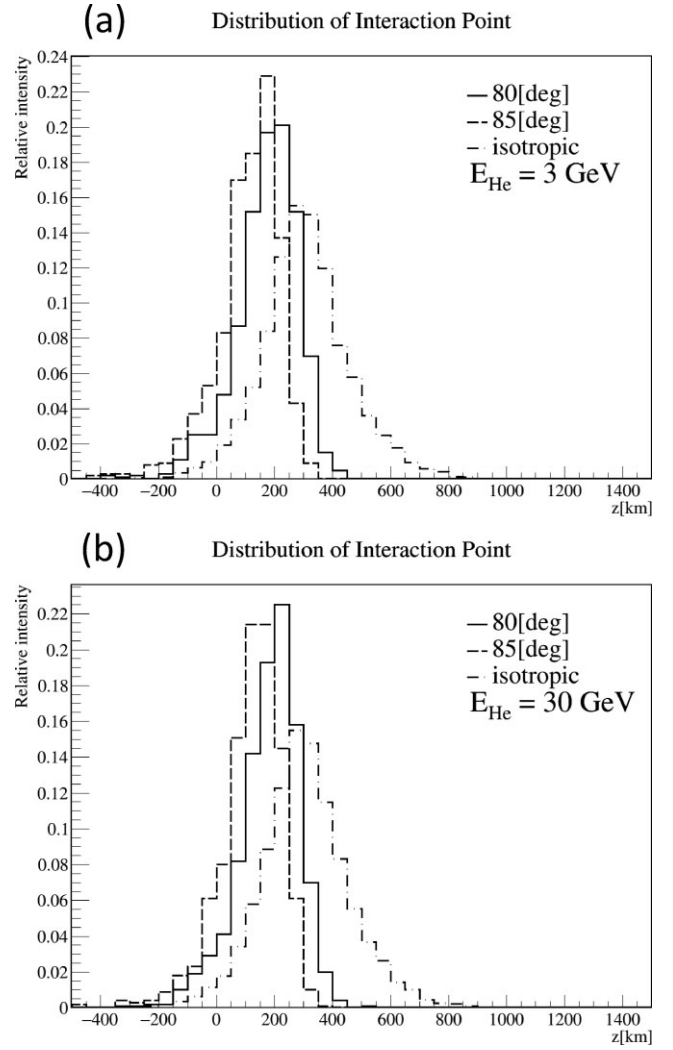


Fig. 27. Same plot as in figure 26, but for the helium ion incidence. The energy of helium ions is fixed at (a) 3 GeV nucleon $^{-1}$ and (b) 30 GeV nucleon $^{-1}$. The magnetic field is assumed to have a non-uniform converging shape. The dash-dotted line curve includes the case of the vertical downward beam without a pitch angle. Concerning vertical entry into the solar atmosphere, the existence of the magnetic field does not affect the results of the peak position. Compared with the proton incidence presented in figure 26, the peak position of the interaction point is shifted toward ≈ 75 km higher altitude than the proton case for incidence at a pitch angle of 85° .

calculation of Hua et al. (2002), the case of $\alpha = 1/5$ was chosen as an example of a converging magnetic field. In the region from 200 km below the photosphere surface to 2500 km above the photosphere, the atmospheric pressure is expressed well by the power law as $P(h > 300-2500 \text{ km}) = 1.08 \times 10^{19} h^{-6.07} \text{ dyn cm}^{-2}$ (Vernazza et al. 1981). In that calculation, h is defined from the altitude of optical thickness 1.0, and h is different from this paper's definition of z . Thus, the magnetic field studied by Hua et al. (2002) is expressed by $B \propto z^{-1.214}$ while the model in this paper is expressed by $B \propto z^{-1.0}$. There is little difference between the two definitions.

$\gamma = -3.0$ isotropic entrance under converging magnetic field

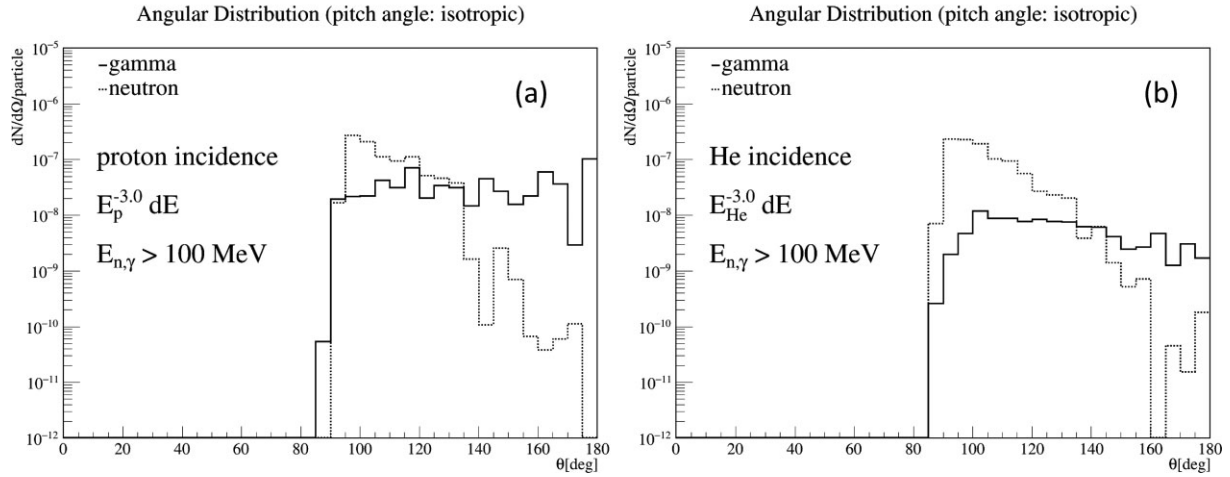


Fig. 28. (a) Expected flux of neutrons (dotted line) and gamma-rays (solid line) induced by the proton beam at the solar surface. The proton beam is assumed to enter the solar surface from the acceleration site with a power index of $\gamma = 3.0$ and downward isotropic pitch angle. The energy spectrum expected by the simulation is made by summing up the secondary gamma-rays and neutrons produced in the solar atmosphere under the condition of appearing from the solar atmosphere with absorption. Therefore, the values could be compared with the results observed using the detectors located either on Earth or onboard the satellites in interplanetary space. (b) Corresponds to the helium incidence in the solar atmosphere under a converging magnetic field. The vertical value represents the flux for $dN/d\Omega$ /helium nucleus. In the calculation, the curvature of the solar atmosphere is taken into account.

$\gamma = -3.0$ 85 degrees under converging magnetic field

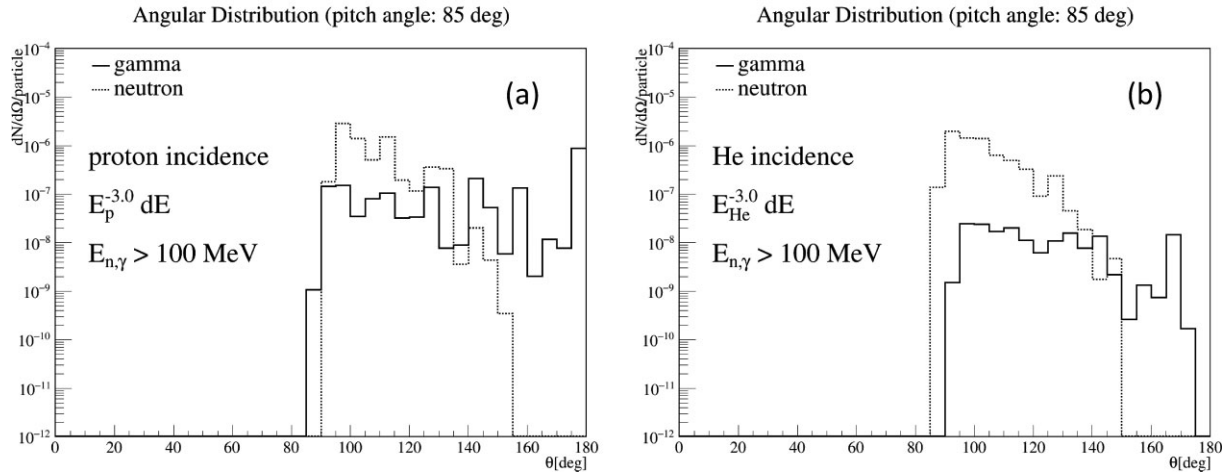


Fig. 29. Same plot as in figure 28, but for entry with a large injection angle such as 85° to the direction of the magnetic field and a power index of $\gamma = 3.0$. (a) Case of proton entry and (b) the case of helium ions. The intensities of neutrons (dashed line) and gamma-rays (solid line) are presented as a function of emission angle from the vertical direction. Note that $\theta = 90^\circ$ and 0° correspond to the solar horizon and vertical direction relative to the solar center, respectively. Therefore, $\theta = 180^\circ$ corresponds to the backward direction. The threshold energy of both neutrons and gamma-rays is set higher than 100 MeV at $E_{n,\gamma} > 100$ MeV. The maximum energy of protons and helium nuclei is set at 30 GeV per nucleus (particles). It is worthwhile to note that, for the helium incidence with 90° – 95° (almost horizontal to the solar surface), such a high n/γ -ratio (≈ 1000) is expected. In the calculation, the curvature of the solar atmosphere is taken into account. The absorption and interactions of gamma-rays and neutrons have also been taken into account.

Figure 17 presents the results under the converging magnetic field. The arrow in figure 17 indicates the point corresponding to the mean free path of protons. The thickness of the atmosphere at the point is about 50 g cm^{-2} or $z = 587 \text{ km}$ below the top of the photosphere.

Figure 25 shows the distribution of collision points of the accelerated protons and helium ions in the solar atmosphere with different pitch angles under a constant magnetic field of 100 G. In contrast, figure 26 shows the distribution of proton interaction under a non-uniform converging

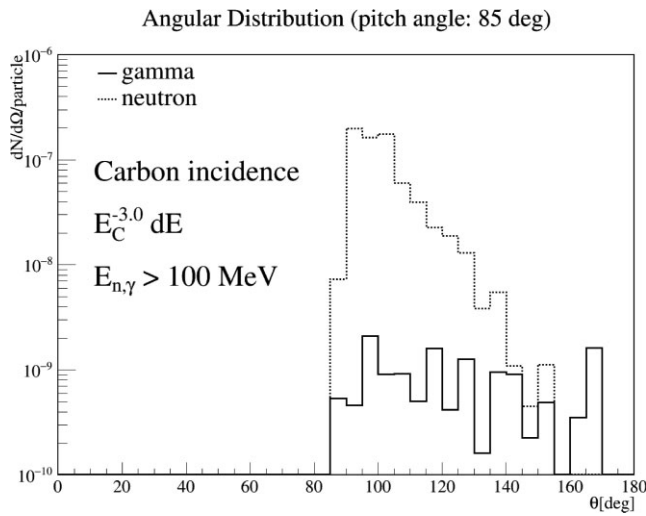


Fig. 30. Same plot as in figures 28 and 29, but for the entry of carbon nuclei with a large injection angle of 85° and with a power index of $\gamma = 3.0$. However, due to the limited computation time in the case of carbon, the maximum energy of each nucleon inside carbon nuclei was limited to 9 GeV. The intensities of neutrons (dashed line) and gamma-rays (solid line) are presented as a function of emission angle from the vertical direction. The curvature of the solar atmosphere is taken into account. The absorption and interactions of gamma-rays and neutrons have also been taken into account.

magnetic field. Figure 27 shows the results for the helium incidence. Generally speaking, when the ions are injected with a large pitch angle such as 85° from the top of the atmosphere ($z = -3000$ km), the interaction point is shifted up about 100 km higher than for isotropic entry. There is no tendency to show any real difference, even in the case of a non-uniform converging magnetic field, when comparing figures 25 and 26.

This research studied actual cases of ion injection with the power energy spectrum of $E^{-\gamma}$. The power indexes (γ) of ions have been changed from 2 to 7, and the abundance of neutrons and high-energy gamma-rays has been investigated. Among those cases, a typical case of $\gamma = 3.0$ is shown in figure 28. (Other cases are shown later, in figures 36 and 37.) This procedure corresponds to the isotropic entry of ions into the solar atmosphere for protons and helium ions as defined by Hua et al. (2002). Figure 29 shows the results calculated for the nearly horizontal entry (85°) at $z = -3000$ km. The proton incidence and helium incidence are shown on the left- and right-hand sides in these figures, respectively. Figure 30 shows a typical feature for the nearly horizontal entry of carbon nuclei. (The energy of the carbon nucleus is given per nucleon, and its maximum energy is limited to 9 GeV due to the limitation of computation time.)

It may be worthwhile to note that when proton incidence is compared with the helium incidence, a high n/γ -ratio such as ≈ 1000 may be expected when the helium beam is directed to 90° – 95° (i.e., almost horizontal [tangential]

Table 1. Main characteristics of the two flares.

Event	A	B
Observation day	2012 June 3	2010 June 12
GOES intensity	M3.3	M2.0
Flare position	N16°E33°	N23°W43°
Flare peak time	17:53:35 UT	00:55:30 UT
LAT γ -rays ($\text{cm}^{-2} \text{s}^{-1}$)	6.4×10^{-4} (10.7σ)	6.5×10^{-3}
2.2 MeV line γ	Weak	Clear
Neutrons (>100 MeV)	47 ± 7	113 ± 23
Statistical significance	4.3σ	5.1σ
Highest neutron	1.2 GeV	2 GeV
Elevation angle	46.1°	43.0°
Amplitude A_1 (event min^{-1})	26 ± 6	27 ± 6
Amplitude A_2 (event min^{-1})	1.6 ± 0.8	1.8
t_0 (min)	29	0

to the solar surface). Here, 0° is defined as the direction toward the solar center.

Figures 31 and 32 show the results of the other cases for protons and helium ions, respectively. The differential energy spectra of neutrons and gamma-rays are shown as a function of the emission angle. Only the energy spectrum is plotted for the incident power index of $\gamma = 3$. As some curves may be useful for future research work, the differential energy spectra of the neutrons and gamma-rays emitted in the forward region (0° – 40°) are presented for values of the incident primary power index γ from 2 to 7 in figures 33 and 34. The calculation also included the curvature of the solar horizon. The threshold energy of secondary neutrons and gamma-rays is set to over $E_{n,\gamma} > 35$ MeV.

6 Comparison with other events

In this section we compare the present event with the other events observed on 2010 June 12 (Ackermann et al. 2012). For simplicity, these events are labeled A for the 2012 June 3 event (SOL2012-06-03) and B for the 2010 June 12 event (SOL2010-06-12). Table 1 lists the main characteristics of each event for comparison. For event A, the energy region of gamma-rays has been extended to a wider energy range, from 10 keV to 600 MeV based on the observation data of FERMI-GBM and LAT. Figure 35 shows the energy spectrum in a wide energy range for the 2012 June 3 event (A).

When events A and B are compared, one first notices that both events have similar characteristics not only in terms of similar gamma-ray intensity and neutron flux at ≥ 100 MeV, but also in terms of forming extremely short impulsive flares. Figure 36 plots the differential energy spectrum of solar neutrons observed on 2010 June 12.

The only difference between the events is that event B was associated with a clear 2.2 MeV gamma-ray line, while the line gamma flux in event A was less intensive,

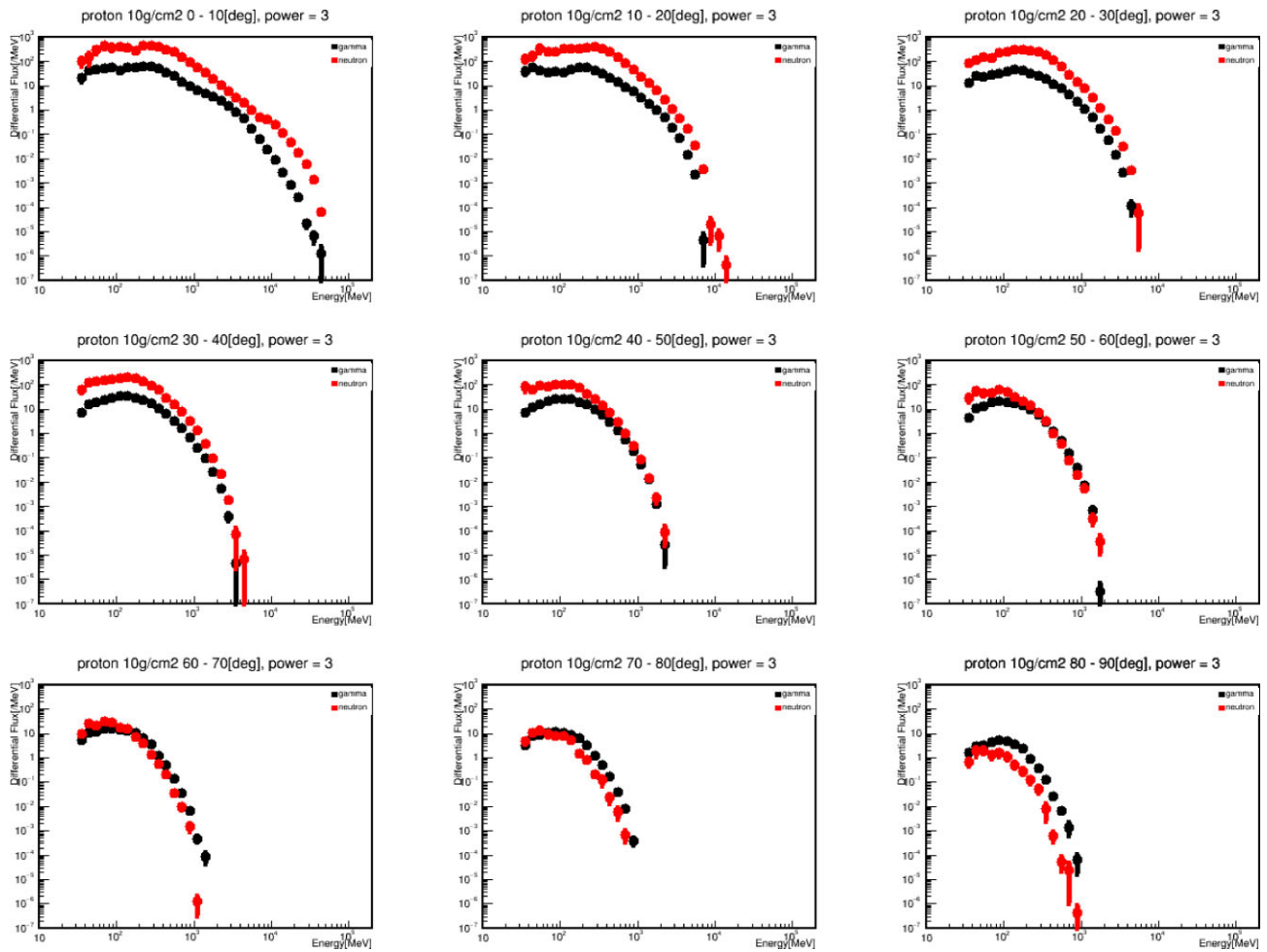


Fig. 31. Differential energy spectra of neutrons (red +) and gamma-rays (black •) at 10 g cm^{-2} presented as a function of the energy of neutrons and gamma-rays and the emission angle. The power index of $\gamma = 3$ is assumed as the energy spectrum of primary protons. The absorption and interactions of gamma-rays and neutrons have been taken into account. (Color online)

as shown in figure 35. The cause of this difference may be attributable to the difference in the crossing angle of the magnetic field line with the photosphere. When the injected ions are forming the fan beam and collide with the solar atmosphere, in the case of the inclined magnetic field shown in figure 37a, the interaction point is expected at a rather shallow region of the photosphere compared to the case of vertical entry.

According to the simulation, in the case of isotropic entry of the proton beam to the solar atmosphere from $z = -3000 \text{ km}$, the most probable interaction point is predicted to be at around $\approx 25 \text{ g cm}^{-2}$ or $z = 440 \text{ km}$, below the border of the photosphere and the chromosphere (figure 17). However, if the ion beam enters the solar atmosphere with the zenith angle of 46.1° (a possible case of A), the most probable interaction point is at $z = 317 \text{ km}$. On the other hand, in the case of vertical entry, secondary neutrons produced by the interaction must penetrate a thicker photosphere

to escape from the solar atmosphere in order to arrive at the Earth. As shown in figure 37a, the difference in the path length to travel through the photosphere between $z = 440 \text{ km}$ and 317 km is estimated to be 177 km [$440 - 317 = 123 \text{ km}$ and $123 \text{ km} / \cos(46.1^\circ) = 177 \text{ km}$]. This implies that in the case of vertical entry, the secondary particles (neutrons) emitted toward the Earth may have a greater chance to collide with the solar atmosphere (figure 37a). In other words, the break-up neutrons of the target nucleus collide with the hydrogen gas and helium nucleus more frequently than in the case of inclined entry and will lose momentum until they reach thermal energy. These low-energy thermal neutrons are the source of the 2.2 MeV line gamma-rays. Nearly thermal energy neutrons collide with the proton gas and form deuterium. Conversely, in the case of inclined entry, such a chance of collision would be less frequently expected, so less-intense 2.2 MeV line gamma-rays would be observed. However, this is an assumption. For deeper

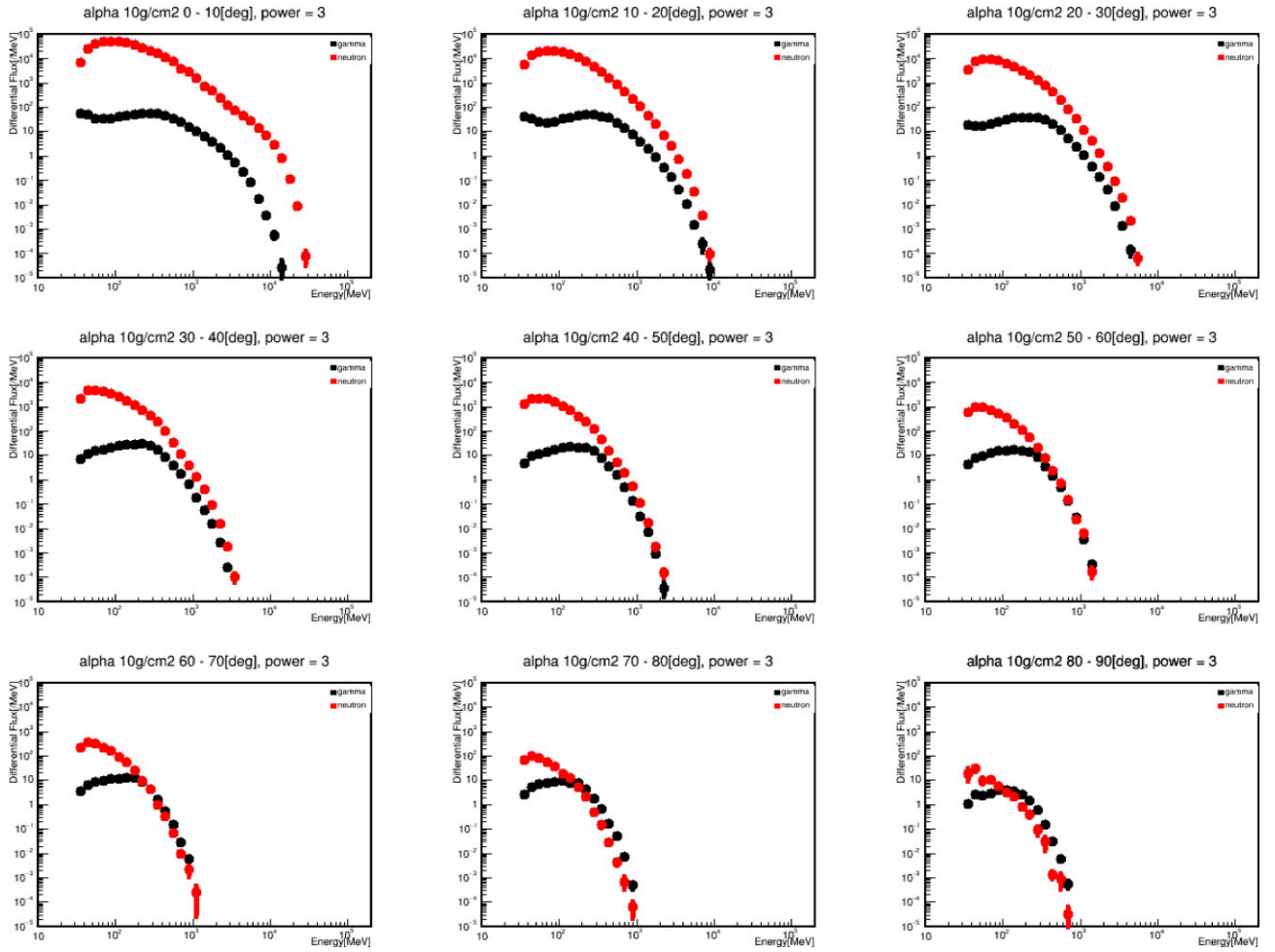


Fig. 32. Same as figure 31, but for the helium incidence. In comparison with the proton incidence, a high production cross-section (high n/γ -ratio) is expected at the cross-section of neutrons over the cross-section of gamma-rays. The absorption and interactions of gamma-rays and neutrons have been taken into account. (Color online)

understanding, we may need a large-scale simulation with use of a super computer. An early work was already made by Ohki in 1990.³

There was an interesting question posed in the paper by Ackerman et al. (2012). They pointed out the possibility of event B being produced by high-energy electrons with an extremely hard spectrum. However, observation of >100 MeV neutrons by the SEDA-FIB suggests another possibility. As shown in figure 35, the change of flux of hard X-rays to a higher energy (as shown by the solid line) passes through a region about two orders of magnitude lower than that of the observed flux of ≈ 100 MeV gamma-rays. Comparing the spectrum of 2012 June 3 (as shown in figure 35 of event A) with the spectrum obtained in the large flare (X10) of 1991 June 15 (Rank et al. 2001), the flux of hard X-rays in the region from 100 keV to

a few MeV is about one order of magnitude higher than that of 1991 June 15. Therefore, the gamma-ray lines of 2.223 MeV and 4.44 MeV might be masked by the intensive gamma-rays induced by the bremsstrahlung process of high-energy electrons. Taking these into account, it would be natural for high-energy gamma-rays of around a few 100 MeV not to be produced by the bremsstrahlung process of electrons with a very hard energy spectrum (i.e., not of leptonic origin), but instead to be produced by the neutral pion production process through ion–ion interactions (i.e., hadronic origin). The observation of neutrons by the SEDA-FIB strongly supports the assumption of the hadronic origin, so the high-energy products observed on 2010 June 12 and 2012 June 6 would be evidence of ion acceleration up to a few GeV.

Finally, we consider the power index evidenced by the measurements of neutrons and gamma-rays in event A. The power index of neutrons in the energy range of

³ Ohki, K. 1990, Lecture in the High Energy Solar Physics group meeting at NAOJ.

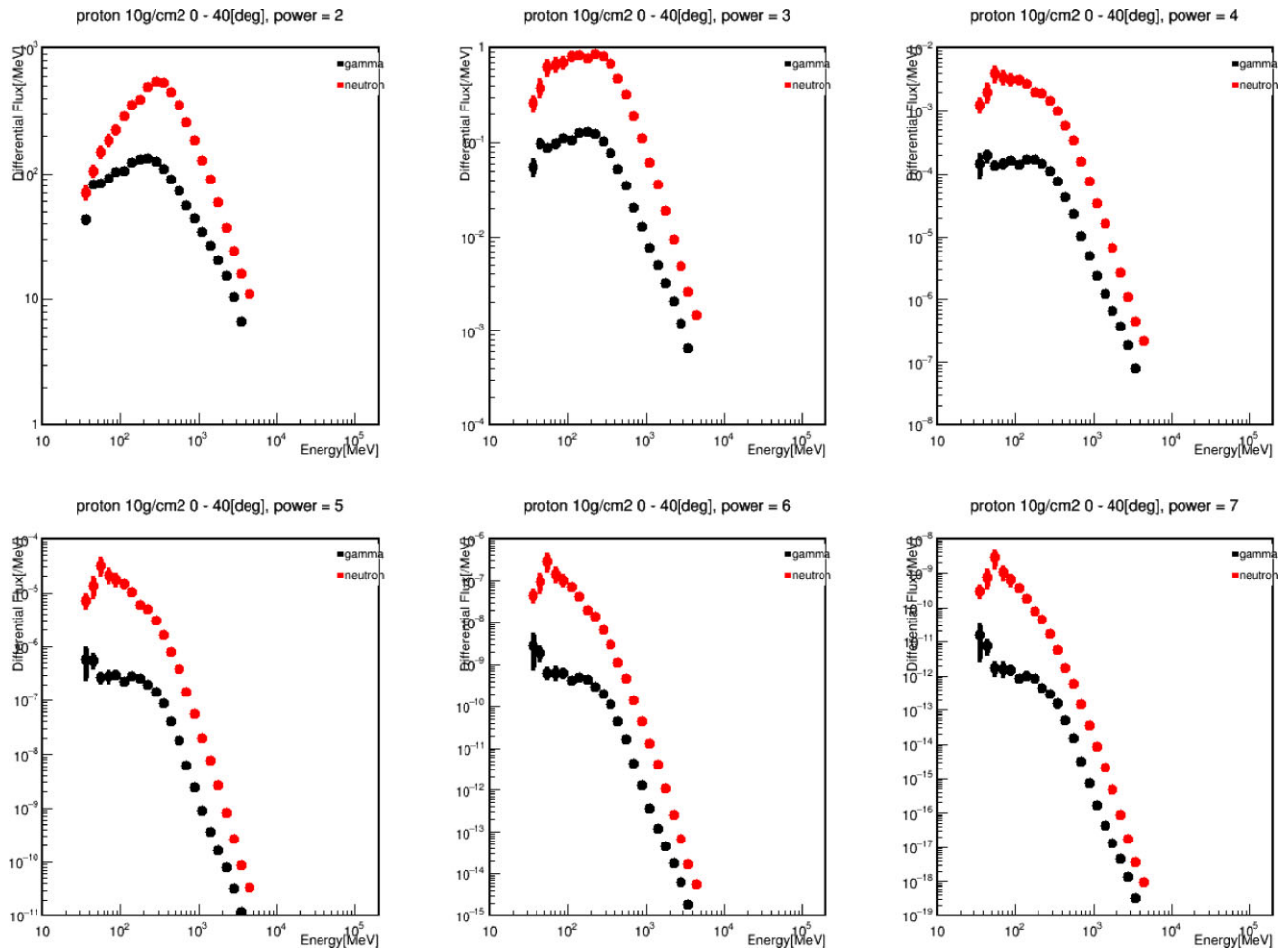


Fig. 33. Differential energy spectra of neutrons (+) and gammas (•) at 10 g cm^{-2} emitted in the forward region ($0^\circ\text{--}40^\circ$) presented as a function of the power index of primary protons with γ from 2 to 7. The absorption and interactions of gamma-rays and neutrons have been taken into account. (Color online)

50–600 MeV is expressed by $\gamma = (2.8 \pm 0.3)$ and the power index of gamma-rays in the energy range of 100–400 MeV can be expressed by $\gamma = (3.3 \pm 0.4)$. However, Share et al. (2018) analyzed the index of protons ($E_p > 300 \text{ MeV}$) as $s = (6.4 \pm 0.4)$. According to the simulation of this report as shown in figures 33 and 34 (for the secondaries emitted within the $0^\circ\text{--}40^\circ$ cone in the forward direction), the slope of neutrons is expected to be $\gamma = 2.7$ in case that the incident protons have the power spectrum with the index of $s = 6$. For the helium incidence, the spectrum of neutrons is expected to have a slightly softer power index of $\gamma = 4$. For example, in the case where helium enters the solar atmosphere with $s = 4$, a power index of $\gamma \approx 3$ is expected for neutrons and a remarkably high n/γ -ratio, such as ≈ 10000 , is expected. This prediction certainly does not match the observed results when a hypothesis of pure helium ion acceleration in the flare is assumed. On the other hand, for the gamma-ray flux, a bump near 200 MeV will be expected due to the two-body decay effect of

neutral pions. From the energy spectrum of gamma-rays in the energy range between 100–1000 MeV, it would thus be difficult to derive the power index of the initial primary ion spectrum. This paper concludes that the results of both analyses are mutually consistent.

The next section will use these MC simulation results in an attempt to depict a possible scenario of the ion acceleration process in the very impulsive flare observed on 2012 June 3.

7 Discussion of the possible acceleration mechanism of ions

The prominent features of the 2012 June 3 event (SOL2012-06-03) may be seen as an extremely short acceleration time and a high n/γ -ratio. Can these features be explained by the results of the Monte Carlo simulation and the shock acceleration theory? This section will discuss this problem.

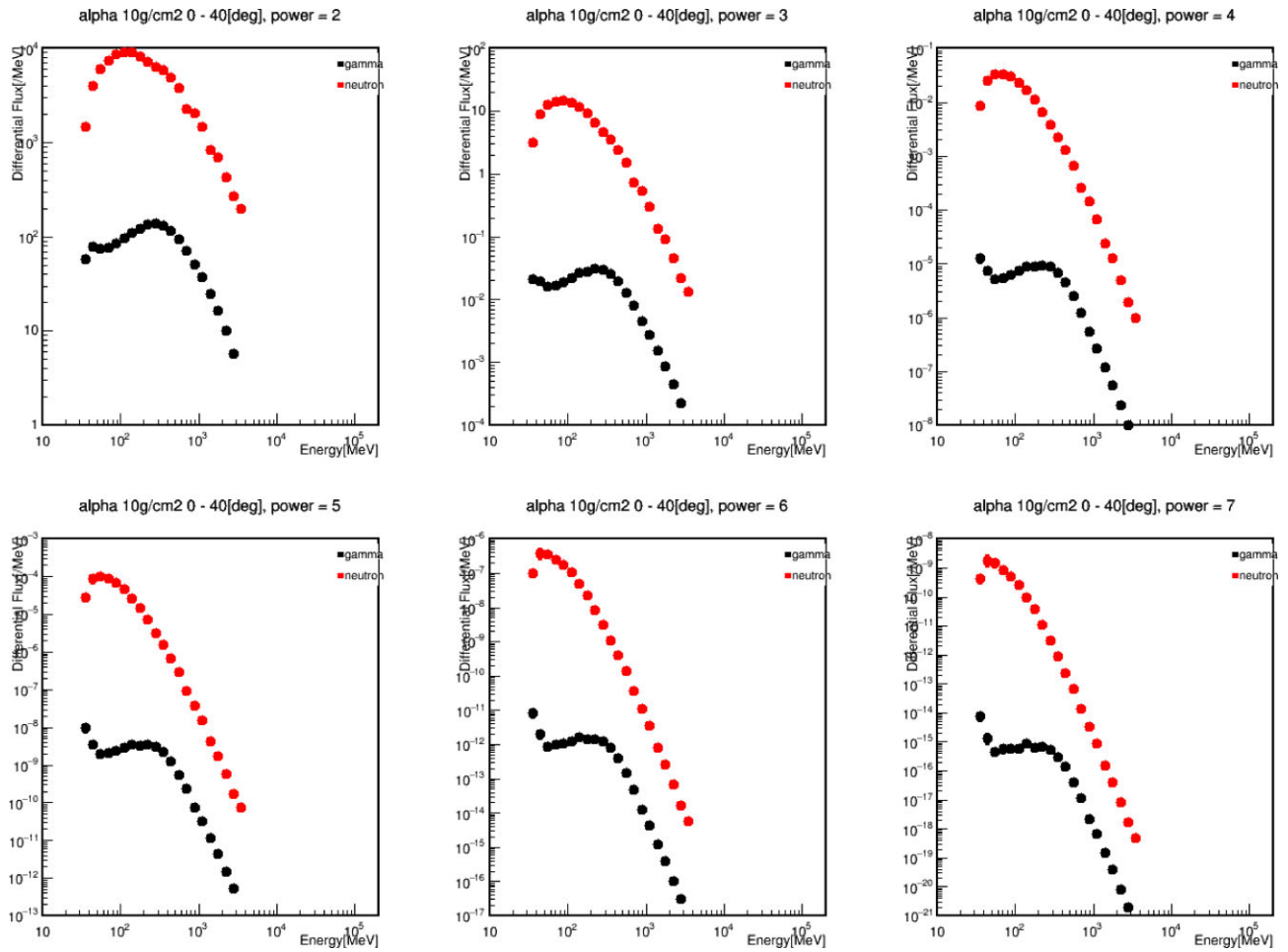


Fig. 34. Differential energy spectra of neutrons (+) and gammas (•) at 10 g cm^{-2} emitted in the forward region (0° – 40°) presented as a function of the power index of primary helium ions with γ from 2 to 7. In comparison with figure 33, the ratio between n and γ is remarkably high. One should be careful with the vertical axis, as it is presented by the logarithmic scale. The absorption and interactions of gamma-rays and neutrons have been taken into account. (Color online)

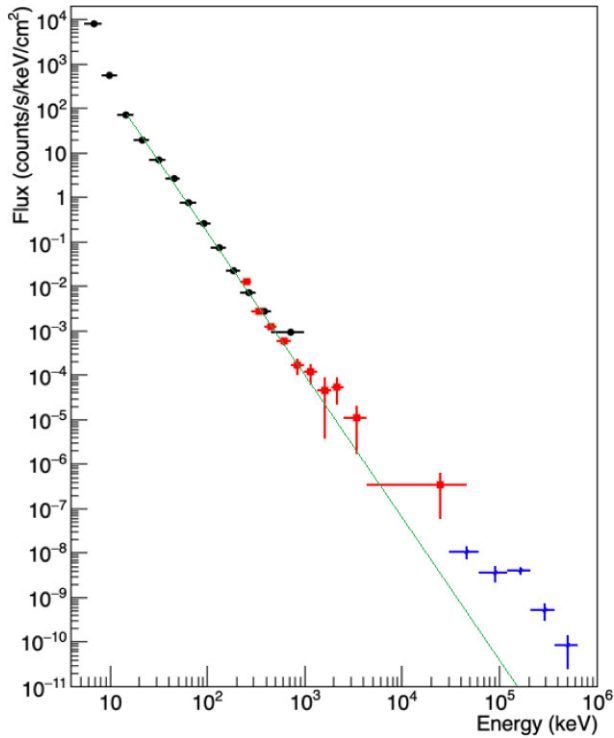
The results of the simulation (shown in figure 22a) suggest that when helium ions are dominantly accelerated and make nuclear interactions at a rather shallow depth in the solar atmosphere (such as $\approx 10 \text{ g cm}^{-2}$), a high n/γ -ratio, such as ≈ 1000 , may be possible. This column density of $\approx 10 \text{ g cm}^{-2}$ of the solar atmosphere corresponds to a solar altitude of about 320 km below the surface of the photosphere (i.e., from the border between the chromosphere and photosphere). Figures 26 and 27 indicate that the most probable interaction point is predicted to be 200 km below the top of the photosphere for helium ions entering the solar atmosphere at an injection angle of 85° to the magnetic field. As shown in figures 28b and 29b, the observed high n/γ -ratio may be explained by the Monte Carlo results. If conditions were realized in the 2012 June 3 flare where helium and C, N, O ions were dominantly injected into the photosphere at a large pitch angle, then the high n/γ -ratio may be explained.

Figure 29 suggests an n/γ -ratio of 1.3 ± 0.4 and 1500 ± 600 for the proton incidence and helium incidence, respectively, when the secondaries are emitted at 90° – 95° (i.e., almost horizontal to the solar surface). This could explain the observed result of the n/γ -ratio as (570 ± 180) , provided that at least 38% of the helium ions in the accelerated particles were involved in those particles.

Figure 29b also suggests that in case the magnetic field line crosses the solar surface at right angles (zenith angle of 0°), the direction of the Earth would in fact correspond to 136° ($= 90^\circ + 46^\circ$), as in the case of the 2012 June 3 event. Therefore, from the data at 136° in figure 29b, the n/γ -ratio is predicted to be around ≈ 1.0 . This would not explain the observed high n/γ -ratio using the vertical entry hypothesis of the field line into the solar photosphere. This is another reason why the inclined magnetic field line that strikes the solar atmosphere with a zenith angle of 46.1° must be considered.

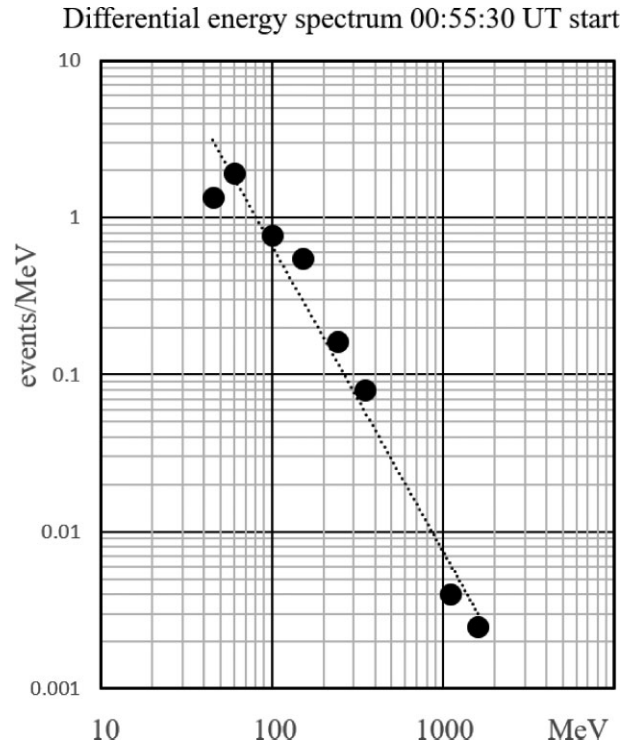
Table 2. Differences between impulsive flares and gradual flares.

Flare type	Impulsive	Gradual
Particles	Electron-rich	Proton-rich
He ³ /He ⁴	≈1	≈0.0005
Fe/O	≈1	≈0.1
H/He	≈10	≈100
Duration	Hours	Days
X-rays	Impulsive	Gradual
Coronagraph		CME (96%)
Solar wind		IP shock
Events/year	≈1000	≈10

**Fig. 35.** Combined energy spectrum of gamma-rays observed by the FERMI-NaI/CsI counter, BGO counter, and LAT counter around 17:53:35 UT. The data of the energy region of 10–300 keV were observed by the NaI/CsI counter, while the data of the energy region of 1–20 MeV were detected by the BGO counter. On the other hand, the data of the 40–600 MeV region were recorded by the LAT calorimeter. We have corrected the acceptance and the detection efficiency of each instrument. The photon data in the energy range between 20 keV and 1 MeV may be well fitted by the power law $E^{-\gamma}$ with $\gamma = 3.3 \pm 0.2$. (Color online)

Reames (1994, 1996) suggested that helium and heavier ions are dominantly involved in impulsive flares, in sharp contrast with gradual flares. Table 2 shows the results of that analysis.

As the present event is an extremely impulsive flare, helium and other heavier ions may have been dominantly accelerated in it. If ions were not dominantly accelerated beyond a few GeV (due to the 293 MeV kinematical limit), the production of neutral pions might be suppressed, and

**Fig. 36.** Differential energy spectrum of solar neutrons observed on 2010 June 12 by the SEDA-FIB. We assumed an instantaneous production of solar neutrons at 00:55:45 UT when the GRB/BGO counter (100–500 keV) started the increase of the counts. For this event, refer to the paper by Ackermann et al. (2012) for details.

may be one reason why such a high n/γ -ratio was observed in the data between the FERMI-LAT and SEDA-FIB detectors.

Let us consider the acceleration time of ions. For example, according to the shock acceleration theory, ions are accelerated every time they pass through the shock front, and gain a small momentum of Δp before being accelerated to high energies. We will define the initial momentum of the ions as P_o , with the ions passing through the shock front n times. After the ions pass through n times, the momentum of ions will be increased to P_n . The rate of momentum gain may be simply expressed by using $\delta = \Delta p/p$ and $P_n = P_o(1 + \delta)^n$. Imagine a situation where the ions are trapped in a magnetic loop, and the shock front is pushing the loop upward (Tsuneta & Naito 1998; Nishizuka & Shibata 2013).

Now look at the solar image taken by the Solar Dynamics Observatory Atmospheric Imaging Assembly (SDO-AIA) telescope at this time (Lemen et al. 2012). The image was taken about one minute before the dominant production of high-energy particles on the solar surface. As shown in figure 38, two hot spots can be recognized at the positions of $(-565'', 292'')$ and $(-560'', 280'')$, indicated by white arrows. The crossing feature of the two loops can be recognized at the two positions on the solar surface

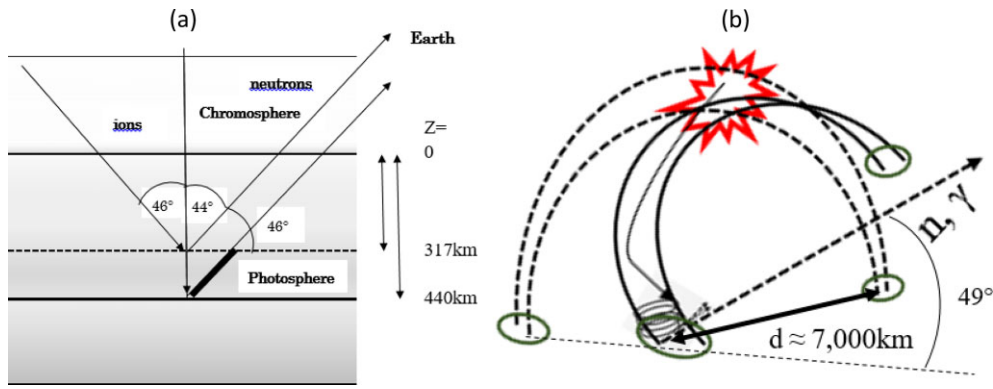


Fig. 37. (a) Difference in the traveling length of neutrons for comparing the vertical incidence and inclined incidence with a zenith angle of 46° . (b) Presents the definition of the geometry used for the calculation. d is defined as the distance between the root of the loop, while loop distance ℓ could be approximated by πr and r is approximated by $r = d/2$. The magnetic loop was approximated as being half of the circle with a radius of $d/2 \approx 3500$ km. (Color online)

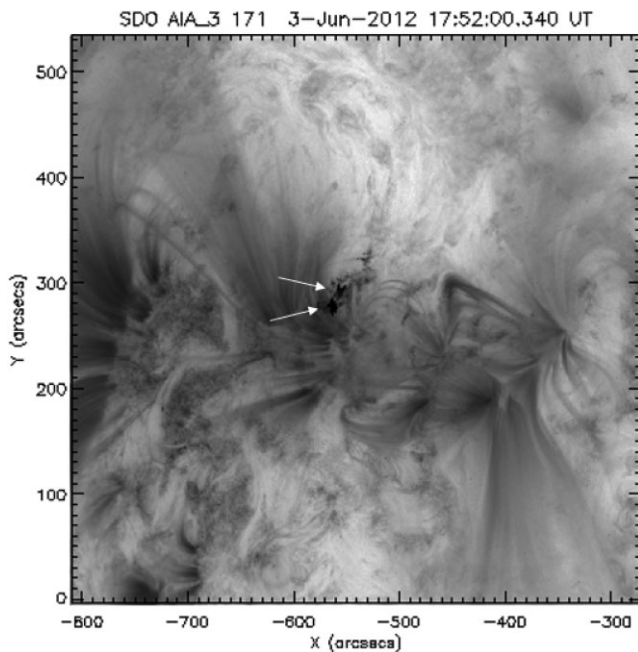


Fig. 38. SDO/AIA images taken by the UV telescope of the 17.1 nm band. This band captures the Fe IX line that corresponds to the temperature of up to one million Kelvin in the transition region of the upper solar atmosphere. The two arrows on the image show the crossing point of the two loops. The coordinates $(-562'', 275'')$ indicated by the bottom arrow correspond to the hot spot observed by the RHESSI satellite (see figure 39). The upper arrow indicates the point at $(-558'', 290'')$.

(Sakai & de Jager 1996). However, as shown in figure 39, the two-dimensional plot of the RHESSI data indicates that the RHESSI hard X-ray hot spot coincides with only one of the coordinates $(-560, 280)$ of the hot spots observed by the SDO-AIA UV telescope.

From figure 38, the loop distance (d) is estimated to be ≈ 7000 km ($\approx 10''$) (figure 37b), so that the half-length of the loop (ℓ) may be estimated to be 10000 to 11000 km ($\approx \pi d/2$). If high-energy particles involved in the loop repeat

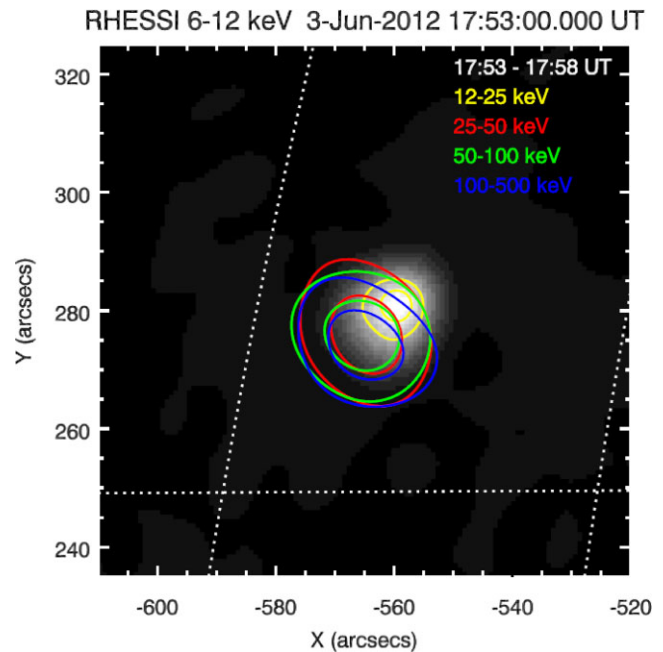


Fig. 39. Two-dimensional plot of hard X-rays for the different bands. The data were imaged by the RHESSI satellite in association with the M3.3 flare on 2012 June 3. Those images were taken in the bands of 12–25 keV (yellow), 25–50 keV (red), 50–100 keV (green), and 100–500 keV (blue). The peak positions are estimated as $(-560'', 281'')$ and $(-565'', 277'')$ for the bands of 12–25 keV and 25–500 keV, respectively. It would be interesting to know whether the peak position differs between the soft X-ray region and the hard X-ray region. (Color online)

the back-and-forth motion inside the magnetic loop, the average collision time (ℓ/c) with the shock front is estimated to be every ≈ 0.035 s. If ions were accelerated within 60 s, the number of times that they pass the shock front may be ≈ 1700 .

Here, if the relative shock speed (Δp) is estimated to be 300 km s^{-1} , the momentum gain $\delta = (4/3) (\Delta p/p)$ would be $1/750$. According to the above equation, $P_n = (1 + \delta)^n$,

P_n turns out to be $(1 + 0.0013)^{1700} \approx 9.1$. Even assuming a fast shock such as 890 km s^{-1} (Share et al. 2018), the value is only estimated to be ≈ 160 . As high-energy gamma-rays were observed in this event, ions must be accelerated up to \approx a few GeV. According to a recent publication by Hoshino (2018), the ions after the reconnection process are expected to have a temperature of $T \approx 70 \text{ keV}$. Therefore, unless warm particles with $T \geq 10 \text{ MeV}$ were not prepared before the acceleration, it would be difficult to explain this event using the standard shock acceleration model.

Another possibility may be sought to explain the main features of this event. An ion acceleration model, such as the DC acceleration model, may be a candidate (Holman 1996). According to Litvinenko and Somov (1995) and Litvinenko (1996), protons and electrons in the reconnection sheet are separated by the electric field induced in the direction perpendicular to the reconnection sheet, due to the difference in the masses of an electron and a proton (Ohsawa & Sakai 1988; Toida & Inagaki 2015). The difference in the Larmor radius between electrons and protons in the anti-parallel magnetic field of the reconnection region is the origin of charge separation in the reconnection sheet. By this charge separation mechanism, an electric field may form inside the reconnection sheet so that electrons and ions are accelerated quickly. According to Litvinenko and Somov (1995), Bogachev and Somov (2005), and Somov (2013), the ion acceleration time to 30 GeV is within $\approx 1 \text{ s}$. The electric field may effectively accelerate the He, C, N, O, and Fe ions due to their high electric charge.

8 Summary and conclusions

In summary, the dominant acceleration of helium and other heavier ions is due to a possibly induced electric field at the reconnection sheets, and the subsequent injection of these particles over the solar atmosphere may explain the very impulsive flare on 2012 June 3 in association with a high n/γ -ratio. Those helium and heavier ions were trapped in the magnetic loop and precipitated over the solar atmosphere with mirroring. Around 320 km below the photosphere surface, in the column density region of $\approx 10 \text{ g cm}^{-2}$, those ions made nuclear interactions and produced gamma-rays and neutrons. The two sensors of the FERMI-LAT and SEDA-FIB, onboard two different spacecraft, detected those high-energy neutrons and high-energy gamma-rays independently. The results reported here represent the best possible effort to-date to characterize the rare phenomenon of the emission of high-energy particles in solar flares. The observations are exploratory and necessarily of fairly low

statistical significance, but they are the best available at the present time.

Acknowledgments

The authors wish to acknowledge the members of the Tsukuba operation center of Kibo for collecting the SEDA-NEM-FIB data every day. We also thank the MAXI team for allowing our use of the data on the solar direction. This work was made possible under the Grant-in-Aid of Scientific Research for Science Research (C) 16K05377 and (A) 21H04468 from the Japan Society for the Promotion of Science. Finally, we want to thank T. Goka and T. Obara for their support of the research and the SEDA-AP mission. The authors thank Prof. Philip Yock of Auckland University and anonymous referee for reading the manuscript very carefully.

References

- Ackermann, M., et al. 2012, *ApJ*, 745, 144
- Atwood, W. B., et al. 2009, *ApJ*, 697, 1071
- Avrett, E. H. 1981, in *Proc. Conf. The Physics of Sunspots*, ed. L. E. Crem & J. H. Thomas (Sunspot, NM: Sacramento Peak Observatory), 235
- Bogachev, S. A., & Somov, B. V. 2005, *Astron. Lett.*, 31, 537
- Cane, H. V. 2000, *Space Sci. Rev.*, 93, 55
- Chupp, E. L. 1971, *Space Sci. Rev.*, 12, 486
- Dorman, L. I. 2010, *Solar Neutrons and Related Phenomena* (Dordrecht: Springer)
- Forbush, S. E. 1946, *Phys. Rev.*, 70, 771
- Holman, G. D. 1996, in *AIP Conf. Proc.*, 374, *High Energy Solar Physics*, ed. R. Ramaty et al. (New York: AIP), 479
- Hoshino, M. 2018, *ApJ*, 868, L18
- Hua, X.-M., & Lingenfelter, R. E. 1987, *ApJ*, 323, 779
- Hua, X.-M., Kozlovsky, B., Lingenfelter, R. E., Ramaty, R., & Stupp, A. 2002, *ApJS*, 140, 563
- Imaida, I., et al. 1999, *Nucl. Instrum. Methods Phys. Res., Sect. A*, 421, 99
- Kamiya, K., et al. 2017, in *Proc. 35th Int. Cosmic Ray Conf., PoS (ICRC2017) (Trieste: SISSA)*, 115
- Koga, K., Goka, T., Matsumoto, H., Obara, T., Muraki, Y., & Yamamoto, T. 2011, *Astrophys. Space Sci. Trans.*, 7, 411
- Koga, K., Muraki, Y., Masuda, S., Shibata, S., Matsumoto, H., & Kawano, H. 2017, *Sol. Phys.*, 292, 115
- Lemen, J. R., et al. 2012, *Sol. Phys.*, 275, 17
- Li, T.-P., & Ma, Y.-Q. 1983, *ApJ*, 272, 317
- Litvinenko, Y. E. 1996, *ApJ*, 462, 997
- Litvinenko, Y. E., & Somov, B. V. 1995, *Sol. Phys.*, 158, 317
- Meegan, C., et al. 2009, *ApJ*, 702, 791
- Miroshnichenko, L. 2015, *Solar Cosmic Rays: Fundamentals and Applications* (Cham: Springer)
- Muraki, Y., et al. 2016, *Sol. Phys.*, 291, 1241
- Muraki, Y., et al. 2020, *PASJ*, 72, 18
- Muraki, Y., Koga, K., Goka, T., Matsumoto, H., Obara, T., Okudaira, O., Shibata, S., & Yamamoto, T. 2012, *Adv. Astron.*, 2012, 379304
- Muraki, Y., Koga, K., Okudaira, O., Shibata, S., Goka, T., Matsumoto, H., Obara, T., & Yamamoto, T. 2013, in *Proc.*

- 33rd International Cosmic Ray Conf. (Red Hook: Curran Associates), 1416
- Murphy, R. J., Kozlovsky, B., Share, G. H., Hua, X.-M., & Lingenfelter, R. E. 2007, *ApJS*, 168, 167
- Nishizuka, N., & Shibata, K. 2013, *Phys. Rev. Lett.*, 110, 051101
- Ohsawa, Y., & Sakai, J.-I. 1988, *ApJ*, 332, 439
- Ramaty, R., Mandzhavidze, N., & Kozlovsky, B. 1996, in *AIP Conf. Proc.*, 374, High Energy Solar Physics (New York: AIP), 172
- Rank, G., Ryan, J., Debrunner, H., McConnell, M., & Schonfelder, V. 2001, *A&A*, 378, 1046
- Reames, D. V. 1994, *Adv. Space Res.*, 15, 41
- Reames, D. V. 1996, in *AIP Conf. Proc.*, 374, High Energy Solar Physics (New York: AIP), 35
- Ryan, J. M., Lockwood, J. A., & Debrunner, H. 2000, *Space Sci. Rev.*, 93, 35
- Sakai, J.-I., & de Jager, C. 1996, *Space Sci. Rev.*, 77, 1
- Share, G. H., Murphy, R. J., White, S. M., Tolbert, A. K., Dennis, B. R., Schwartz, R. A., Smart, D. F., & Shea, M. A. 2018, *ApJ*, 869, 182
- Somov, B. V. 2013, *Plasma Astrophysics, Part II: Reconnection and Flares* (New York: Springer Science), 392
- Toida, M., & Inagaki, J. 2015, *Phys. Plasmas*, 22, 062305
- Tsuneta, S., & Naito, T. 1998, *ApJ*, 495, L67
- Vernazza, J. E., Avrett, E. H., & Loeser, R. 1981, *ApJS*, 45, 635
- Zweibel, E. G., & Haber, D. A. 1983, *ApJ*, 264, 648